Preprint accepted for publication in AIAA Journal of Guidance, Control, and Dynamics (Version: April 17, 2019)

Control of a Drag Power Kite over the Entire Wind Speed Range

Florian Bauer[*], Daniel Petzold[†], and Ralph M. Kennel[‡]
Chair of Electrical Drive Systems and Power Electronics, Technical University of Munich, Arcisstrasse 21, 80333 Munich, Germany

Filippo Campagnolo[§]
Wind Energy Institute, Technical University of Munich, Boltzmannstrasse 15, 85748 Garching, Germany

Roland Schmehl[¶]
Kite Power Research Group, Aerospace Engineering Faculty at Delft University of Technology, Kluyverweg 1, 2629 HS Delft, The Netherlands

A control scheme for drag power kites, also known as airborne wind turbines, for the entire wind speed range is proposed, including (i) a temperature controller allowing for temporary overloading of the powertrain, (ii) a limitation controller ensuring that power-, force-, speed-, and actuator constraints are satisfied, (iii) a tangential flight speed controller, and (iv) a tangential force control allocation, which inverts the nonlinearities of the plant and allocates the flight speed controller's tangential force demand to the available actuators. The drag power kite plant model is based on a point-mass model and a simple aerodynamics model with various drag contributions. Simulations are conducted with the parameters of the 20 kW Wing 7 developed by Makani Power, Inc. The proper working of the control scheme is indicated by the good match of the simulation results with independent simulation results and measurements published by Makani. A temporary overloading of the powertrain with about twice the nominal power can be concluded as a requirement, otherwise the mean power would be significantly lower. Due to the reduction of the lift and thus reduction of the centripetal force at high wind speeds, the inside-down figure eight can be concluded as the best pattern.

---

[*] Florian Bauer is a Ph.D. candidate at the Chair of Electrical Drive Systems and Power Electronics, Technical University of Munich, Arcisstrasse 21, 80333 Munich, Germany; florian.bauer@tum.de; corresponding author.

[†] Daniel Petzold graduated as M.Sc. from the Chair of Electrical Drive Systems and Power Electronics, Technical University of Munich, Arcisstrasse 21, 80333 Munich, Germany; daniel.petzold@tum.de.

[‡] Ralph M. Kennel is Professor at the Chair of Electrical Drive Systems and Power Electronics, Technical University of Munich, Arcisstrasse 21, 80333 Munich, Germany; ralph.kennel@tum.de.

[§] Filippo Campagnolo is a postdoc researcher at the Wind Energy Institute, Technical University of Munich, Boltzmannstrasse 15, 85748 Garching, Germany; filippo.campagnolo@tum.de.

[¶] Roland Schmehl is Associate Professor with the Kite Power Research Group, Aerospace Engineering Faculty at Delft University of Technology, Kluyverweg 1, 2629 HS Delft, The Netherlands; r.schmehl@tudelft.nl

I. Introduction

Kites are tethered wings and promising alternatives to harvest wind energy, cf. e.g. [1–6]. The considered kite has onboard wind turbines to generate electrical power which is transmitted to the ground via electrical cables integrated in the tether [7, 8]. Due to the high flight speed of the kite, the airflow speed at the kite is about a magnitude higher than the actual wind speed, which allows for a rather small size of the onboard turbines. For vertical take-off and subsequent transition into crosswind flight, the turbines are used as propellers. This procedure is reversed for the landing when the wind calms down or for maintenance. This airborne wind energy concept is called "crosswind kite power/drag power" [1], or sometimes also "onboard power generation", "continuous power generation", "fly-gen", or "airborne wind turbine".

Compared to conventional wind turbines, crosswind kite power promises to harvest wind energy at higher altitudes with stronger and steadier winds, but by requiring only a fraction of the construction material. Hence, it promises to have lower capital costs and in the end a lower Levelized Cost of Electricity. A drag power kite with a nominal electrical power of 20 kW ("Wing 7") was developed by the company Makani Power Inc. (in the following denoted in short by "Makani") and demonstrated autonomously power generation as well as launching and landing [9, 10]. Currently, a larger scale 600 kW system ("M600") is being developed [9, 11–13].

The development of a drag power kite plant is challenging. One important aspect is the control of the kite. Many researchers proposed Nonlinear Model Predictive Control for this task, cf. e.g. [2, 5, 14–20]. A drawback is the high computational load. Researchers also developed more conventional controllers, cf. e.g. [21–23]. Fagiano et al. [24] proposed a proportional controller on a control-oriented submodel to track the kite's flight trajectory, which was then used and extended by others, cf. e.g. [25]. Further studies target a maximum power point tracking-like approach to optimize the power generation, cf. e.g. [26, 27].

However, all currently available controllers are incomplete for drag power kites and particularly do not consider the entire wind speed range from no wind to cut-out wind. The present study aims at closing this gap, summarizing the contributions as follows: (i) Derivation of a drag power kite plant model, suitable for controller derivations. (ii) Derivation and proposal of a control method, which controls the kite over the entire wind speed range. This particularly includes (ii-a) a temperature controller allowing for temporary overloading of the powertrain, (ii-b) a limitation controller ensuring that power-, force-, speed-, and actuator constraints are satisfied, (ii-c) a tangential flight speed controller, and (ii-d) a tangential force control allocation, which inverts the nonlinearities of the plant and allocates the flight speed controller's tangential force demand to the available actuators. (iii) Validation of the control method by means of dynamic simulations and comparison of results to simulations and measurements conducted by Makani.

The kite's modeling approach is similar to the point-mass model proposed by Fechner [25] (see also references therein), but has a number of extensions which are in part adapted from [28, 29]. The derived model and subsequently the derived controllers apply to crosswind flight. Launching, landing, transitions, and failures e.g. of rotors are not considered. Nevertheless, it is shown that the model's fidelity is sufficient for the purpose of this study.

This paper is organized as follows: Sect. II derives the model equations and Sect. III proposes the control scheme. Sect. IV gives details on the simulation implementation. Sect. V reports simulation results and validates the model with measurements of the Makani Wing 7. Sect. VI gives concluding remarks.

II. Model Derivation

A. Point-Mass Dynamics

Recalling Newton's axioms, with the assumption of a constant mass, and translational kinematics, one obtains

$$\dot{\boldsymbol{v}}_\mathrm{k} = m_\mathrm{a}^{-1}\boldsymbol{F}_\mathrm{acc}, \qquad \boldsymbol{v}_\mathrm{k}(t_0) = \boldsymbol{v}_\mathrm{k,0}, \tag{1}$$

$$\dot{\boldsymbol{r}}_\mathrm{k} = \boldsymbol{v}_\mathrm{k}, \qquad \boldsymbol{r}_\mathrm{k}(t_0) = \boldsymbol{r}_\mathrm{k,0}, \tag{2}$$

$$\boldsymbol{F}_\mathrm{acc} = \sum_i \boldsymbol{F}_i = \boldsymbol{F}_\mathrm{g} + \boldsymbol{F}_\mathrm{te} + \boldsymbol{F}_\mathrm{a}, \tag{3}$$

where $\boldsymbol{v}_\mathrm{k}$ is the kite's velocity with initial value $\boldsymbol{v}_\mathrm{k,0}$ at initial time t_0, $\boldsymbol{r}_\mathrm{k}$ is the kite's position with initial value $\boldsymbol{r}_\mathrm{k,0}$, m_a is the effective airborne mass, $\boldsymbol{F}_\mathrm{acc}$ is the acceleration force acting on the kite, which is also the sum of all (external) forces $\boldsymbol{F}_i$ acting on the kite, with gravitational force $\boldsymbol{F}_\mathrm{g}$, tether force $\boldsymbol{F}_\mathrm{te}$, and aerodynamic force $\boldsymbol{F}_\mathrm{a}$. All vectors are given in the flat-earth inertial reference frame, which is here defined by the right-handed north-west-up Cartesian axes for the $\boldsymbol{x}$-$\boldsymbol{y}$-$\boldsymbol{z}$ base vectors with origin at the ground station tether connection projected to the flat-earth (i.e. origin has zero altitude above ground).

B. Forces

The gravitational force can be expressed with the gravitational acceleration g as

$$\boldsymbol{F}_\mathrm{g} = m_\mathrm{a}(0, 0, -g)^\top. \tag{4}$$

The tether is modeled as a massless spring-damper in the tether extend direction if under tension (see e.g. [25, 30, 31] for details on tether modeling approaches). The force magnitude of the tether spring-damper (index "sd") is given by

$$F_\mathrm{te,sd} = \varsigma_\mathrm{te}\mathit{\Delta} r_\mathrm{te} + \xi_\mathrm{te}\mathit{\Delta} v_\mathrm{te}, \tag{5}$$

where ς_{te} is the spring constant, ξ_{te} is the damper constant, $\mathit{\Delta} r_{\mathrm{te}}$ is the elongation

$$\mathit{\Delta} r_{\mathrm{te}} = ||\boldsymbol{r}_{\mathrm{k}} - \boldsymbol{r}_{\mathrm{gs}}|| - L_{\mathrm{te}} \tag{6}$$

with the ground station's tether connection position (index "gs") $\boldsymbol{r}_{\mathrm{gs}}$, the (unstrained) tether length L_{te}, and where $\mathit{\Delta} v_{\mathrm{te}}$ is the elongation speed defined by

$$\mathit{\Delta} v_{\mathrm{te}} = \boldsymbol{e}_{\mathrm{r}} \bullet \boldsymbol{v}_{\mathrm{k}} \tag{7}$$

with radial direction $\boldsymbol{e}_{\mathrm{r}} = \mathrm{dir}(\boldsymbol{r}_{\mathrm{k}} - \boldsymbol{r}_{\mathrm{gs}})$. Herein, $||\boldsymbol{x}||$ is the Euclidian norm of some vector $\boldsymbol{x}$, $\bullet$ is the dot product, and the direction of a vector $\boldsymbol{x}$ is defined by

$$\mathrm{dir}(\boldsymbol{x}) := \begin{cases} \boldsymbol{x}/||\boldsymbol{x}|| & \text{for } ||\boldsymbol{x}|| \neq 0, \\ \boldsymbol{0} & \text{otherwise.} \end{cases} \tag{8}$$

As the tether can only exert a tension force, the tether force vector is given by

$$\boldsymbol{F}_{\mathrm{te}} = \begin{cases} -\boldsymbol{e}_{\mathrm{r}} F_{\mathrm{te,sd}} & \text{if } \mathit{\Delta} r_{\mathrm{te}} > 0 \text{ and } F_{\mathrm{te,sd}} > 0 \\ \boldsymbol{0} & \text{otherwise.} \end{cases} \tag{9}$$

The aerodynamic force is generally given by

$$\boldsymbol{F}_{\mathrm{a}} = \boldsymbol{F}_{\mathrm{L}} + \boldsymbol{F}_{\mathrm{D}} + \boldsymbol{F}_{\mathrm{S}} \tag{10}$$

with lift-, drag-, and side force

$$\boldsymbol{F}_{\mathrm{L}} = \frac{1}{2}\rho v_{\mathrm{a}}^2 A C_{\mathrm{L}} \,\mathrm{dir}(\boldsymbol{v}_{\mathrm{a}} \times \boldsymbol{y}_{\mathrm{k}}), \tag{11}$$

$$\boldsymbol{F}_{\mathrm{D}} = \frac{1}{2}\rho v_{\mathrm{a}}^2 A C_{\mathrm{D}} \,\mathrm{dir}(\boldsymbol{v}_{\mathrm{a}}), \tag{12}$$

$$\boldsymbol{F}_{\mathrm{S}} = \frac{1}{2}\rho v_{\mathrm{a}}^2 A C_{\mathrm{S}} \,\mathrm{dir}(\boldsymbol{F}_{\mathrm{D}} \times \boldsymbol{F}_{\mathrm{L}}), \tag{13}$$

where $C_{\mathrm{L}}, C_{\mathrm{D}}, C_{\mathrm{S}}$ are the lift-, drag-, and side coefficients, ρ is the air density, v_{a} is the airflow speed, A is the kite's reference area (projected wing area), $\boldsymbol{y}_{\mathrm{k}}$ is the y-axis base vector of the kite-fixed reference frame which points along the wing span into the starboard direction, and × denotes the cross product.

C. Airflow Speed

The airflow speed is given by $v_\mathrm{a} = ||\boldsymbol{v}_\mathrm{a}||$ with the airflow velocity vector

$$\boldsymbol{v}_\mathrm{a} = \boldsymbol{v}_\mathrm{w}(\boldsymbol{r}_\mathrm{k}) - \boldsymbol{v}_\mathrm{k}, \tag{14}$$

where $\boldsymbol{v}_\mathrm{w}(\boldsymbol{r}_\mathrm{k})$ is the wind velocity at the position (or altitude) of the kite. That wind velocity is $\boldsymbol{v}_\mathrm{w}(\boldsymbol{r}_\mathrm{k}) = \boldsymbol{R}_\mathrm{z}(\varphi_\mathrm{w})\,(v_\mathrm{w}, 0, 0)^\top$ where φ_w is the azimuth angle of the wind (i.e. the azimuth of the wind direction w.r.t. the north or the $\boldsymbol{x}$ unit vector of the inertial reference frame) and v_w is the wind speed at the kite. Herein, rotation matrices $\boldsymbol{R}_i(\#)$ for rotations around a x-, y-, and z-axis (i) about some angle # are defined using the right hand rule. The wind speed v_w in the altitude of the kite above ground $h = \boldsymbol{z} \bullet \boldsymbol{r}_\mathrm{k}$ (i.e. at the kite's position) is modeled by $v_\mathrm{w} = (h/h_\mathrm{ref})^{\alpha_\mathrm{H}} v_{\mathrm{w},h_\mathrm{ref}}$, where $v_{\mathrm{w},h_\mathrm{ref}}$ is the wind speed in the reference altitude above ground h_ref, and α_H is the Hellmann exponent, cf. e.g. [32, p. 9ff.] or [33].

D. Kite Reference Frame/Kite Orientation

The kite's reference frame is defined as follows: The x-axis base vector $\boldsymbol{x}_\mathrm{k}$ points from the nose to the tail, the y-axis base vector $\boldsymbol{y}_\mathrm{k}$ points along the main wing span into the starboard direction, and the z-axis base vector $\boldsymbol{z}_\mathrm{k}$ points up. By implication, a point-mass has no defined orientation, but assuming that angle of attack α, angle of sideslip β, and roll angle ψ (angle between tether and vertical kite axis) are stabilized instantaneously through according horizontal and vertical stabilizers or/and through underlying control loops, the kite's orientation can be modeled as follows: With $\alpha = 0$, $\beta = 0$, and $\psi = 0$ (in the following: orientation with prime), it is implied that $\boldsymbol{x}'_\mathrm{k}$ is parallel to $\boldsymbol{v}_\mathrm{a}$, and $\boldsymbol{y}'_\mathrm{k}$ is perpendicular to both $\boldsymbol{v}_\mathrm{a}$ and the tether radial direction $\boldsymbol{e}_\mathrm{r}$. Finally, $\boldsymbol{z}'_\mathrm{k}$ is perpendicular to both $\boldsymbol{x}'_\mathrm{k}$ and $\boldsymbol{y}'_\mathrm{k}$. This results in

$$\boldsymbol{x}'_\mathrm{k} = \mathrm{dir}(\boldsymbol{v}_\mathrm{a}), \qquad \boldsymbol{y}'_\mathrm{k} = \mathrm{dir}(\boldsymbol{e}_\mathrm{r} \times \boldsymbol{v}_\mathrm{a}), \qquad \boldsymbol{z}'_\mathrm{k} = \boldsymbol{x}'_\mathrm{k} \times \boldsymbol{y}'_\mathrm{k}. \tag{15}$$

Those vectors can be combined to the transformation matrix

$$\boldsymbol{T}'_\mathrm{k} = \begin{pmatrix} \boldsymbol{x}'_\mathrm{k} & \boldsymbol{y}'_\mathrm{k} & \boldsymbol{z}'_\mathrm{k} \end{pmatrix}, \tag{16}$$

with which any vector given in the kite's primed reference frame (at $\alpha = 0$, $\beta = 0$, $\psi = 0$) can be transformed into inertial reference frame. For arbitrary α, β, and ψ, the orientation is given again by the analogy of transforming any vector from the kite's reference frame (denoted by $\#^\mathrm{k}$) into inertial reference frame: $\#^\mathrm{k}$ is first rotated by β about the z-axis, then by α about the y-axis, and then by ψ about the x-axis, before it is transformed with $\boldsymbol{T}'_\mathrm{k}$, hence

$$\begin{pmatrix} \boldsymbol{x}_\mathrm{k} & \boldsymbol{y}_\mathrm{k} & \boldsymbol{z}_\mathrm{k} \end{pmatrix} = \boldsymbol{T}_\mathrm{k} = \boldsymbol{T}'_\mathrm{k} \boldsymbol{R}_\mathrm{x}(\psi) \boldsymbol{R}_\mathrm{y}(\alpha) \boldsymbol{R}_\mathrm{z}(\beta). \tag{17}$$

To avoid to define the lift-, drag-, and side force coefficients as function of α and β, but instead to use a simplified model for the aerodynamic coefficients, the following two assumptions are made: (i) Angle of attack α and angle of sideslip β are either both kept at zero (controlled by underlying control loops and/or empennage), or their effects are only implicitly covered via according values of the aerodynamic coefficients. (Note that a zero kite angle of attack does not mean a zero airfoil/wing angle of attack due to an angle of incidence unequal to zero.) (ii) The side force coefficient is always zero. This allows to set $\alpha = 0$ and $\beta = 0$ in (17) which simplifies to

$$\begin{pmatrix} \boldsymbol{x}_\mathrm{k} & \boldsymbol{y}_\mathrm{k} & \boldsymbol{z}_\mathrm{k} \end{pmatrix} = \boldsymbol{T}_\mathrm{k} = \boldsymbol{T}'_\mathrm{k} \boldsymbol{R}_\mathrm{x}(\psi), \tag{18}$$

and the side force (13) is zero and (10) simplifies to

$$\boldsymbol{F}_\mathrm{a} = \boldsymbol{F}_\mathrm{L} + \boldsymbol{F}_\mathrm{D}. \tag{19}$$

E. Total Lift and Drag Coefficients

The contributions to the total lift and drag coefficients C_L and C_D originate from the kite's airframe, from the tether, and from the rotors, i.e. generally

$$C_\mathrm{L} = C_\mathrm{L,k} + C_\mathrm{L,te} + C_\mathrm{L,rot}, \tag{20}$$

$$C_\mathrm{D} = \underbrace{C_\mathrm{D,k} + C_\mathrm{D,te}}_{=:\, C_\mathrm{D,eq}} + C_\mathrm{D,rot}, \tag{21}$$

where index "k" is for kite (or its airframe), index "te" is for tether, and index "rot" is for rotors, and where the sum of $C_\mathrm{D,k}$ and $C_\mathrm{D,te}$ is also called equivalent drag coefficient $C_\mathrm{D,eq}$.

The kite's main wing usually dominates the lift contribution, hence $C_\mathrm{L,te} = 0$, and $C_\mathrm{L,rot} = 0$ with which (20) becomes

$$C_\mathrm{L} = C_\mathrm{L,k} = C_\mathrm{L,k,mw} \tag{22}$$

where $C_\mathrm{L,k,mw}$ is the total lift coefficient of the main wing.

The rotor drag coefficient $C_\mathrm{D,rot}$ is considered as a steerable actuation.

Adopted from [15, 16, 29, 30, 34–37], the tether drag contribution is modeled by

$$C_\mathrm{D,te} = \frac{1}{4} \frac{d_\mathrm{te} L_\mathrm{te}}{A} c_\mathrm{D,te}, \tag{23}$$

where d_{te} is the tether's frontal width (which is the tether's diameter for the considered cylindrical tether design as in [8]), $c_{\mathrm{D,te}}$ is the drag coefficient of the tether's cross section shape (which is here a circle), and L_{te} is the tether length.

The contributions to the kite's drag coefficient originate from the main wing and other kite parts such as fuselage and empennage. Moreover, it is considered that the kite's drag can be steered via an actuation e.g. by air brakes. The kite's total drag coefficient is therefore generally given by

$$C_{\mathrm{D,k}} = C_{\mathrm{D,k,mw}} + C_{\mathrm{D,k,o}} + C_{\mathrm{D,k,a}}, \tag{24}$$

where index "mw" is for main wing, index "o" is for other parts, and index "a" is for actuation.

Herein, the drag of other parts $C_{\mathrm{D,k,o}}$ is assumed as fixed value and the actuated drag $C_{\mathrm{D,k,a}}$ is assumed as actuation steerable within the range $C_{\mathrm{D,k,a}} \in [C_{\mathrm{D,k,a,min}}, C_{\mathrm{D,k,a,max}}]$, where $C_{\mathrm{D,k,a,min}} = 0$ and $C_{\mathrm{D,k,a,max}}$ are the fixed minimum and maximum steerable values.

For the main wing's lift and drag coefficients, $C_{\mathrm{L,k,mw}}$ and $C_{\mathrm{D,k,mw}}$, a solution from lifting line theory is adopted,

$$C_{\mathrm{L,k,mw}} = \frac{c_{\mathrm{L}}}{1 + 2/\mathit{Æ}} \tag{25}$$

$$C_{\mathrm{D,k,mw}} = C_{\mathrm{D,k,mw,p}} + C_{\mathrm{D,k,mw,i}} \tag{26}$$

$$C_{\mathrm{D,k,mw,p}} = c_{\mathrm{D}} \tag{27}$$

$$C_{\mathrm{D,k,mw,i}} = \frac{C_{\mathrm{L,k,mw}}^2}{\pi e \mathit{Æ}} \tag{28}$$

$$\mathit{Æ} = b^2/A \tag{29}$$

where c_{L} and c_{D} are the lift and drag coefficients of the main wing's airfoil (i.e. 2D), $C_{\mathrm{D,k,mw,p}}$ is the main wing's parasitic drag, $C_{\mathrm{D,k,mw,i}}$ is the main wing's induced drag, $\mathit{Æ}$ is the main wing's aspect ratio, e is the main wing's span efficiency, and b is the main wing's span (cf. e.g. [38, p. 167ff.]). Eqs. (25)–(29) imply the assumption that aerodynamic interferences e.g. between wings and rotors are negligible or can be modeled with appropriate values for e and $C_{\mathrm{D,k,o}}$.

Finally, the airfoil lift and drag coefficients are related: Apart from stall, the drag coefficient of an airfoil (also called profile drag) increases approximately quadratically with the airfoil's lift coefficient. Hence, for $c_{\mathrm{L}} \in [c_{\mathrm{L,min\text{-}op}}, c_{\mathrm{L,max\text{-}op}}]$ with minimum and maximum operationally allowed lift coefficients $c_{\mathrm{L,min\text{-}op}}$ and $c_{\mathrm{L,max\text{-}op}}$, which are both before stall including a safety margin, the airfoil's drag coefficient can be modeled by

$$c_{\mathrm{D}} = c_{\mathrm{D},0} + c_{\mathrm{D},2} c_{\mathrm{L}}^2, \tag{30}$$

where $c_{\mathrm{D},0}$ is the airfoil's drag coefficient at $c_{\mathrm{L}} = 0$ and $c_{\mathrm{D},2}$ is the drag coefficient slope w.r.t. the lift coefficient squared. The maximum operational airfoil lift coefficient is also defined as the nominal airfoil lift coefficient, $c_{\mathrm{L,max\text{-}op}} =: c_{\mathrm{L,n}}$. Here, c_{L} is considered as actuation. Changes of c_{L} may originate e.g. from control surface deflections.

F. Actuators

The only considered actuations, with which the kite can be controlled, are (i) the rotor drag coefficient $C_{\mathrm{D,rot}}$, (ii) the airfoil lift coefficient c_{L}, (iii) the actuated drag coefficient $C_{\mathrm{D,k,a}}$, and (iv) the roll angle ψ. The dynamics of each of the four actuators is modeled as limited first order delay. Thus, for an actuation $u \in [C_{\mathrm{D,rot}}, c_{\mathrm{L}}, C_{\mathrm{D,k,a}}, \psi]$,

$$\dot{u} = \frac{1}{T_u}[\mathrm{limit}(u_{\mathrm{min}}, u_{\mathrm{set}}, u_{\mathrm{max}}) - u], \qquad u(t_0) = u_0, \tag{31}$$

where T_u is the actuation time constant, u_{set} is the actuation set value, u_{min} and u_{max} are the minimum and maximum actuation values, u_0 is the initial value, and

$$\mathrm{limit}(u_{\mathrm{min}}, u_{\mathrm{set}}, u_{\mathrm{max}}) := \begin{cases} u_{\mathrm{min}} & \text{if } u_{\mathrm{set}} < u_{\mathrm{min}}, \\ u_{\mathrm{max}} & \text{if } u_{\mathrm{set}} > u_{\mathrm{max}}, \\ u_{\mathrm{set}} & \text{otherwise} \end{cases} \tag{32}$$

implements actuator constraints.

G. Powertrain

With the definition of the rotor drag coefficient $C_{\mathrm{D,rot}}$ in (21), the rotors' thrust force is

$$F_{\mathrm{rot}} = \frac{1}{2}\rho v_{\mathrm{a}}^2 A C_{\mathrm{D,rot}} \tag{33}$$

and their power, which is here called "aerodynamic power", is

$$P_{\mathrm{a}} = v_{\mathrm{a}} F_{\mathrm{rot}} = \frac{1}{2}\rho v_{\mathrm{a}}^3 A C_{\mathrm{D,rot}}. \tag{34}$$

Generative power is defined positive while consumed[1] power is defined negative.

A temporary overloading of the powertrain might be crucial due to significant power oscillations within the crosswind flight trajectory, see also [39]. Powertrains can usually be overloaded for some time in the order of seconds or tens of seconds with a maximum overloading power in the order of twice the nominal power, until the nominal temperature of a

---

[1] Physically, power cannot be consumed but only converted. The wordings "consumed" and "consumptive" are used here for sake of brevity as alternative e.g. for "from the grid demanded" power.

powertrain component is reached, cf. e.g. [40]. Here, the simplest possible temperature dynamics model is employed through a single time constant, cf. e.g. [40, Sect. III]. The model can be formulated in per unit by

$$\dot{\tau}' = \frac{1}{T_\tau}(P'_{\mathrm{loss}} - \tau' + \tau'_\infty), \qquad \tau'(t_0) = \tau'_0, \tag{35}$$

where

$$\tau' = (\tau - \tau_{\infty,\mathrm{n}})/(\tau_\mathrm{n} - \tau_{\infty,\mathrm{n}}) \tag{36}$$

is the per unit temperature with initial value τ'_0 at initial time t_0, absolute temperature τ, nominal absolute temperature τ_n, and nominal ambient temperature $\tau_{\infty,\mathrm{n}}$; T_τ is the temperature time constant [40];

$$\tau'_\infty = (\tau_\infty - \tau_{\infty,\mathrm{n}})/(\tau_\mathrm{n} - \tau_{\infty,\mathrm{n}}) \tag{37}$$

is the per unit ambient temperature with absolute ambient temperature τ_∞; and

$$P'_{\mathrm{loss}} = \begin{cases} P_\mathrm{a}/P_{\mathrm{a},+,\mathrm{n}} & \text{if } P_\mathrm{a} \geq 0, \\ P_\mathrm{a}/P_{\mathrm{a},-,\mathrm{n}} & \text{otherwise} \end{cases} \tag{38}$$

is the per unit power loss in the powertrain (or its most critical component such as an electrical machine) with nominal generative and consumptive power $P_{\mathrm{a},+,\mathrm{n}}$ and $P_{\mathrm{a},-,\mathrm{n}}$[2], respectively.

H. Sensors, Control Computers, Communications

For the purpose of deriving and validating a first control approach, all states and intermediate values of the model are assumed to be available exactly to the controllers, i.e. without noise or delay. It is further assumed that control algorithms are executed quasi-continuous, i.e. the inverse of the control frequency is much smaller than the smallest time constant of the plant, and that communications delays are negligible.

I. Control Problem Formulation

The derived drag power kite plant model is a system of explicit nonlinear ordinary differential equations with eleven states (velocity $\boldsymbol{v}$ in x-y-z, position $\boldsymbol{r}$ in x-y-z, the four actuations $C_{\mathrm{D,rot}}$, c_L, $C_{\mathrm{D,k,a}}$, ψ, and the temperature τ'). It remains to derive controllers. This control problem can be formulated as follows: Find a control scheme which, over the entire wind speed range, (i) keeps the aerodynamic power P_a, the lift force F_L, the airflow speed v_a, the temperature τ', and the

---

[2] Note that $|P_{\mathrm{a},+,\mathrm{n}}|$ may differ significantly from $|P_{\mathrm{a},-,\mathrm{n}}|$ due to critical components or nonlinearities within the powertrain.

actuations $C_{\mathrm{D,rot}}$, c_{L}, $C_{\mathrm{D,k,a}}$, ψ within their limits, (ii) stabilizes the kite on a circular or figure eight flight path, and (iii) harvests power optimally.

III. Proposed Control Method

Figure 1 illustrates the proposed control scheme. Indices "min", "max", and "set" are for the minimum, maximum, and set values, $P_{\mathrm{a},+,\mathrm{max}\text{-}\tau}$ and $P_{\mathrm{a},-,\mathrm{max}\text{-}\tau}$ are the maximum generative and consumptive aerodynamic powers to satisfy the temperature limits, and $F_{\mathrm{tan,set}}$ is the set value of the tangential force. Those latter three quantities are introduced within the corresponding control part derivation in the following subsections. The utilized flight path controller is an extension of Fagiano's approach [24], which allows for arbitrary paths including circles and inside-up figure eights. For sake of brevity (space restriction), the flight path controller is not elaborated in this paper.

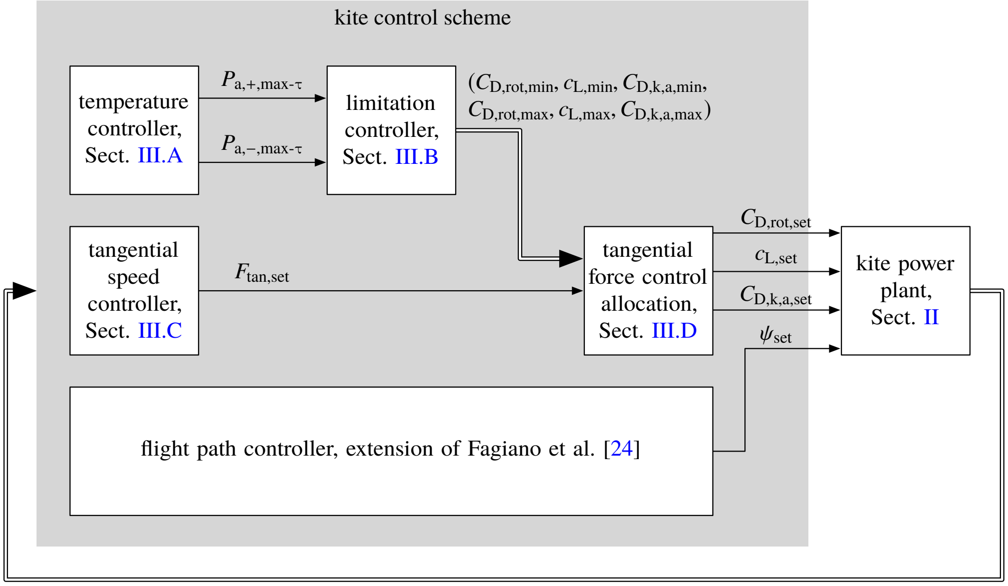

Figure 1 Block diagram of the proposed kite control scheme.

A. Temperature Controller

1. Controller Equations

The temperature controller is designed with the following rationale: It controls the powertrain's temperature to its nominal temperature with the virtual actuation P_{a}, cf. (35) with (38). However, instead of applying the virtual actuation P_{a} directly, only a "maximum value" is computed, one for generative power $P_{\mathrm{a},+,\mathrm{max}\text{-}\tau}$ and one for consumptive power $P_{\mathrm{a},-,\mathrm{max}\text{-}\tau}$. Only in the case if the tangential force control allocation needs a high power (indirectly over $C_{\mathrm{D,rot,set}}$, cf. Fig. 1), then $P_{\mathrm{a},+,\mathrm{max}\text{-}\tau}$ or $P_{\mathrm{a},-,\mathrm{max}\text{-}\tau}$, respectively, may indeed be actuated.

A proportional controller is chosen with "proportional pre-filter" and "disturbance" cancelation of τ'_{∞} to avoid a steady-state error. Moreover, as the purpose of the temperature control is to reduce the instantaneous power $|P_{\mathrm{a}}|$ from its instantaneous maximum $P_{\mathrm{a,+,max}}$ or $|P_{\mathrm{a,-,max}}|$ down to its nominal value $P_{\mathrm{a,+,n}}$ or $P_{\mathrm{a,-,n}}$ if the temperature limit is reached, a feedforward of the maximum instantaneous power is applied. Finally, the controller's output is limited to the maximum instantaneous power. Hence, the controller equations are

$$\mathit{\Delta}\tau' = G_{\mathrm{F},\tau}\tau'_{\mathrm{set}} - \tau' \tag{39}$$

$$P_{\mathrm{a,+,max}\text{-}\tau} = \mathrm{limit}(0\,,\; G_{\mathrm{P},\tau}\mathit{\Delta}\tau' - P_{\mathrm{a,+,n}}\tau'_{\infty} + P_{\mathrm{a,+,max}}\;,\; P_{\mathrm{a,+,max}}) \tag{40}$$

$$|P_{\mathrm{a,-,max}\text{-}\tau}| = \mathrm{limit}(0\,,\; G_{\mathrm{P},\tau}\mathit{\Delta}\tau' - |P_{\mathrm{a,-,n}}|\tau'_{\infty} + |P_{\mathrm{a,-,max}}|\,,\; |P_{\mathrm{a,-,max}}|) \tag{41}$$

where $\mathit{\Delta}\tau'$ is the temperature error, τ'_{set} is the set value of the temperature (which is the nominal temperature in per unit, i.e. $\tau'_{\mathrm{set}} = 1$), $G_{\mathrm{P},\tau}$ is the proportional gain, and $G_{\mathrm{F},\tau}$ is the "proportional pre-filter". The use of absolute values, denote by $|\#|$, is for sake of simplicity, such that no signs have to be changed.

Figure 2 shows the block diagram of the temperature control loop. The grey part is the controller. The "actual set value"-block models that $P_{\mathrm{a,+,max}\text{-}\tau}$ or $P_{\mathrm{a,-,max}\text{-}\tau}$ may not directly be the set-value which is selected by the tangential force control allocation (indirectly over $C_{\mathrm{D,rot,set}}$). Because of that and because at the end only a single P_{a} value is actually set, Eqs. (40) and (41) can be combined to the short form

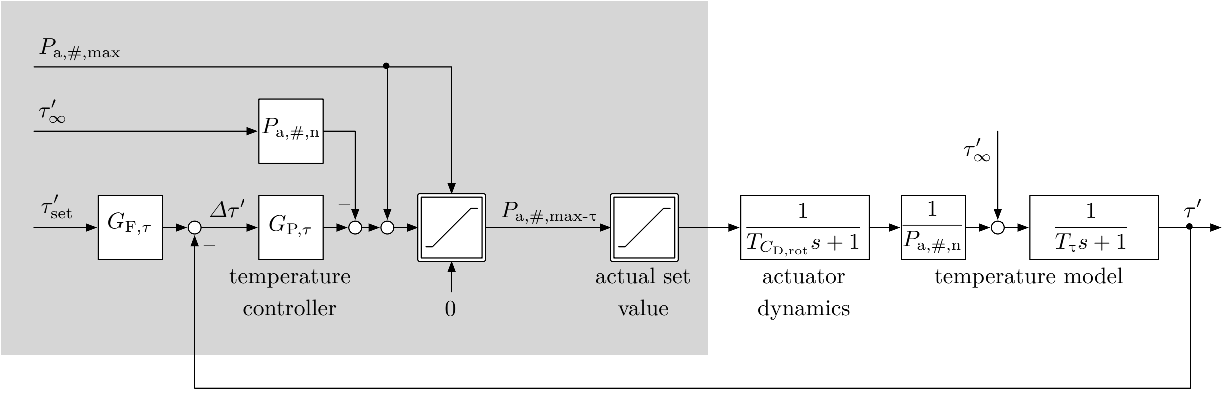

Figure 2 Block diagram of the temperature control loop.

$$P_{\mathrm{a},\#,\mathrm{max}\text{-}\tau} = \mathrm{limit}(0\,,\; G_{\mathrm{P},\tau}\mathit{\Delta}\tau' - P_{\mathrm{a},\#,\mathrm{n}}\tau'_{\infty} + P_{\mathrm{a},\#,\mathrm{max}}\,,\; P_{\mathrm{a},\#,\mathrm{max}}) \tag{42}$$

with

$$\begin{pmatrix} P_{\mathrm{a},\#,\mathrm{max}\text{-}\tau} & P_{\mathrm{a},\#,\mathrm{max}} & P_{\mathrm{a},\#,\mathrm{n}} \end{pmatrix} = \begin{cases} \begin{pmatrix} P_{\mathrm{a,+,max}\text{-}\tau} & P_{\mathrm{a,+,max}} & P_{\mathrm{a,+,n}} \end{pmatrix} & \text{for generative,} \\ \begin{pmatrix} |P_{\mathrm{a,-,max}\text{-}\tau}| & |P_{\mathrm{a,-,max}}| & |P_{\mathrm{a,-,n}}| \end{pmatrix} & \text{for consumptive.} \end{cases} \tag{43}$$

The other blocks in Fig. 2 are a visualization of (31), (35), (39), and (42), where the linear-dynamic subparts are written in the Laplace-domain with complex frequency s. The representation of Fig. 2 is also used in the following for the controller parametrization.

2. *Aerodynamic Power Limits*

The maximum instantaneous (overloading) generative aerodynamic power can be defined by

$$P_{\mathrm{a},+,\mathrm{max}} = f_{\text{over-P}} P_{\mathrm{a},+,\mathrm{n}} \tag{44}$$

with power overloading (or underloading) factor $f_{\text{over-P}}$. The value of $f_{\text{over-P}}$ depends on the overloading capability of the powertrain (or its most critical component). Similarly to (44), the maximum instantaneous (overloading) consumptive aerodynamic power, or minimum instantaneous (overloading) aerodynamic power, can be defined by

$$P_{\mathrm{a},-,\mathrm{max}} = f_{\text{over-P}} P_{\mathrm{a},-,\mathrm{n}}. \tag{45}$$

3. *Controller Parametrization and Stability*

In view of Fig. 2, the linearized closed loop input-output behavior (i.e. the limitation blocks become 1) is given by

$$\begin{aligned} \tau' &= \frac{1}{T_\tau s + 1}\left\{\tau'_\infty + \frac{1}{P_{\mathrm{a},\#,\mathrm{n}}}\frac{1}{T_{C_{\mathrm{D,rot}}} s + 1}\left[P_{\mathrm{a},\#,\mathrm{max}} - P_{\mathrm{a},\#,\mathrm{n}}\tau'_\infty + G_{\mathrm{P},\tau}\left(G_{\mathrm{F},\tau}\tau'_{\mathrm{set}} - \tau'\right)\right]\right\} \\ \Leftrightarrow \qquad &= \frac{\frac{P_{\mathrm{a},\#,\mathrm{n}}}{P_{\mathrm{a},\#,\mathrm{n}}+G_{\mathrm{P},\tau}} T_{C_{\mathrm{D,rot}}} s\tau'_\infty + \frac{P_{\mathrm{a},\#,\mathrm{max}}}{P_{\mathrm{a},\#,\mathrm{n}}+G_{\mathrm{P},\tau}} + \frac{G_{\mathrm{F},\tau}}{\frac{P_{\mathrm{a},\#,\mathrm{n}}}{G_{\mathrm{P},\tau}}+1}\tau'_{\mathrm{set}}}{\frac{P_{\mathrm{a},\#,\mathrm{n}} T_{C_{\mathrm{D,rot}}} T_\tau}{P_{\mathrm{a},\#,\mathrm{n}}+G_{\mathrm{P},\tau}} s^2 + \frac{P_{\mathrm{a},\#,\mathrm{n}}(T_{C_{\mathrm{D,rot}}}+T_\tau)}{P_{\mathrm{a},\#,\mathrm{n}}+G_{\mathrm{P},\tau}} s + 1}. \end{aligned} \tag{46}$$

The control loop is stable if the denominator polynomial has positive coefficients, being a 2nd order Hurwitz polynomial.

The controller is parametrized by pole-placement by comparing the denominator of (46) with that of a second order delay

$$T_\#^2 s^2 + 2D_\# T_\# s + 1 \tag{47}$$

with time constant $T_\# > 0$ (which is the inverse of the eigen angular frequency, $\omega_\# = T_\#^{-1}$) and damping $D_\# > 0$ (which is sometimes also denoted by $\zeta_\#$): The closed temperature control loop time constant $T_\# = T_{\tau,\circ}$ and damping $D_\# = D_{\tau,\circ}$ are then defined by the two equations

$$T_{\tau,\circ}^2 = \frac{P_{\mathrm{a},\#,\mathrm{n}} T_{C_{\mathrm{D,rot}}} T_\tau}{P_{\mathrm{a},\#,\mathrm{n}} + G_{\mathrm{P},\tau}}, \tag{48}$$

$$2D_{\tau,\circ}T_{\tau,\circ} = \frac{P_{\mathrm{a},\#,\mathrm{n}}(T_{C_{\mathrm{D,rot}}} + T_\tau)}{P_{\mathrm{a},\#,\mathrm{n}} + G_{\mathrm{P},\tau}}. \tag{49}$$

There is only one degree of freedom, $G_{\mathrm{P},\tau}$, so the control designer chooses $T_{\tau,\circ}$ or $D_{\tau,\circ}$. Here, the latter is used, for which $G_{\mathrm{P},\tau}$ is given by squaring (49), substituting (48), and solving for $G_{\mathrm{P},\tau}$:

$$G_{\mathrm{P},\tau} = P_{\mathrm{a},\#,\mathrm{n}}\left[\frac{(T_{C_{\mathrm{D,rot}}} + T_\tau)^2}{4D_{\tau,\circ}^2 T_{C_{\mathrm{D,rot}}} T_\tau} - 1\right]. \tag{50}$$

The steady-state value can be determined by setting $s = 0$ in (46), which results in

$$\tau' = \frac{P_{\mathrm{a},\#,\mathrm{max}}}{P_{\mathrm{a},\#,\mathrm{n}} + G_{\mathrm{P},\tau}} + \frac{G_{\mathrm{F},\tau}}{\frac{P_{\mathrm{a},\#,\mathrm{n}}}{G_{\mathrm{P},\tau}} + 1}\tau'_{\mathrm{set}}. \tag{51}$$

Because $\tau' = \tau'_{\mathrm{set}}$ shall be achieved for steady-state, the prefilter $G_{\mathrm{F},\tau}$ must be

$$\tau'_{\mathrm{set}} = \frac{P_{\mathrm{a},\#,\mathrm{max}}}{P_{\mathrm{a},\#,\mathrm{n}} + G_{\mathrm{P},\tau}} + \frac{G_{\mathrm{F},\tau}}{\frac{P_{\mathrm{a},\#,\mathrm{n}}}{G_{\mathrm{P},\tau}} + 1}\tau'_{\mathrm{set}} \qquad \Leftrightarrow G_{\mathrm{F},\tau} = 1 + \frac{1}{G_{\mathrm{P},\tau}}\left(P_{\mathrm{a},\#,\mathrm{n}} - \frac{P_{\mathrm{a},\#,\mathrm{max}}}{\tau'_{\mathrm{set}}}\right). \tag{52}$$

Note that both, $G_{\mathrm{P},\tau}$ and $G_{\mathrm{F},\tau}$, may differ for the two power flow directions.

B. Limitation Controller

The limitation controller outputs the actuations limits of $C_{\mathrm{D,rot}}$, c_{L}, and $C_{\mathrm{D,k,a}}$ (cf. Fig. 1) with which (i) not only the actuator limits are satisfied, but also (ii) the maximum instantaneous power limits are satisfied, (iii) the powertrain temperature limit is satisfied, and (iv) the force limits (lift force; tether force and further forces implicitly) are satisfied.

1. Rotor Drag Coefficient Upper Limit

The temperature controller outputs the maximum aerodynamic power $P_{\mathrm{a},+,\mathrm{max}\text{-}\tau}$ (40), which satisfies both, the temperature limit and the maximum instantaneous power (44). The upper limit for $C_{\mathrm{D,rot}} = C_{\mathrm{D,rot,max}}$ is readily given by substituting $P_{\mathrm{a}} = P_{\mathrm{a},+,\mathrm{max}\text{-}\tau}$ into (34) and rearranging to

$$P_{\mathrm{a},+,\mathrm{max}\text{-}\tau} = \frac{1}{2}\rho v_{\mathrm{a}}^3 A C_{\mathrm{D,rot,max}} \qquad \Leftrightarrow \frac{P_{\mathrm{a},+,\mathrm{max}\text{-}\tau}}{\frac{1}{2}\rho v_{\mathrm{a}}^3 A} = C_{\mathrm{D,rot,max}}, \tag{53}$$

where v_{a} is the currently measured/identified airflow speed.

2. Rotor Drag Coefficient Lower Limit

Analogously to (53), the lower limit of the rotor drag coefficient is given by

$$P_{\text{a},-,\text{max-}\tau} = \frac{1}{2}\rho v_\text{a}^3 A C_{\text{D,rot,min}} \qquad \Leftrightarrow \frac{P_{\text{a},-,\text{max-}\tau}}{\frac{1}{2}\rho v_\text{a}^3 A} = C_{\text{D,rot,min}}. \tag{54}$$

3. Airfoil Lift Coefficient Lower Limit

The minimum feasible airfoil lift coefficient is already defined through $c_{\text{L,min-op}}$.

Moreover, the lift force has some lower bound $F_{\text{L,min}}$ such that the kite remains airborne (cf. [28, 29]). The corresponding minimal airfoil lift coefficient is given by inserting $F_\text{L} = F_{\text{L,min}}$ and (22) with (25) into the magnitude of (11) and solving for $c_\text{L} = c_{\text{L,min-F}}$, which is

$$F_{\text{L,min}} = \frac{1}{2}\rho v_\text{a}^2 A \frac{c_{\text{L,min-F}}}{1+\frac{2}{\textit{Æ}}} \qquad \Leftrightarrow c_{\text{L,min-F}} = \frac{F_{\text{L,min}}\left(1+\frac{2}{\textit{Æ}}\right)}{\frac{1}{2}\rho v_\text{a}^2 A}. \tag{55}$$

Hence, ultimately the lower bound for the airfoil lift coefficient is

$$c_{\text{L,min}} := \max\{c_{\text{L,min-op}}, c_{\text{L,min-F}}\}. \tag{56}$$

4. Airfoil Lift Coefficient Upper Limit

A first upper bound for c_L is the nominal lift coefficient $c_{\text{L,n}} = c_{\text{L,max-op}}$.

A second upper bound for c_L is given via the maximum instantaneous lift force $F_{\text{L,max}}$, which is

$$F_{\text{L,max}} = f_{\text{over-F}} F_{\text{L,n}} \tag{57}$$

with force overloading (or underloading) factor $f_{\text{over-F}}$ and nominal lift force $F_{\text{L,n}}$, that is the force for which the kite and tether etc. are designed for. Analogously to (55), the maximum airfoil lift coefficient due to force limitations is

$$c_{\text{L,max-F}} = \frac{F_{\text{L,max}}\left(1+\frac{2}{\textit{Æ}}\right)}{\frac{1}{2}\rho v_\text{a}^2 A}. \tag{58}$$

To satisfy all upper limits, the maximum airfoil lift coefficient is

$$c_{\text{L,max}} = \min\left\{c_{\text{L,n}}, c_{\text{L,max-F}}\right\}. \tag{59}$$

Because the currently measured/identified airflow speed v_a is used in (58), it cannot be excluded that $c_\mathrm{L,max} < c_\mathrm{L,min}$ during transients, e.g. if there is a gust. To avoid that contradiction, the maximum airfoil lift coefficient also has the minimum airfoil lift coefficient as a lower bound and (59) is replaced by

$$c_\mathrm{L,max} = \max\left\{\min\left\{c_\mathrm{L,n}, c_\mathrm{L,max\text{-}F}\right\}, c_\mathrm{L,min}\right\}. \tag{60}$$

5. Actuated Drag Coefficient Limits

The limits of $C_\mathrm{D,k,a}$ are already defined in Sect. II.E through $C_\mathrm{D,k,a,min}$ and $C_\mathrm{D,k,a,max}$.

C. Tangential Speed Controller

1. Tangential Direction and Tangential Dynamics

The speed controller is designed for the "tangential" kite dynamics, i.e. the dynamics in the flight direction tangential to the sphere spanned by the tether. This direction can be defined by

$$\boldsymbol{e}_\mathrm{tan} := \boldsymbol{e}_\mathrm{cen} \times \boldsymbol{e}_\mathrm{r}, \qquad \text{with } \boldsymbol{e}_\mathrm{cen} := \mathrm{dir}(\boldsymbol{e}_\mathrm{r} \times \boldsymbol{v}_\mathrm{k}) \tag{61}$$

(where $\boldsymbol{e}_\mathrm{cen}$ is the centripetal direction in left turns or centrifugal direction in right turns, respectively). Assuming that the tangential direction is approximately parallel to the kite's velocity $\boldsymbol{e}_\mathrm{tan}||\boldsymbol{v}_\mathrm{k}$, then the kite's tangential dynamics is given by

$$\dot{v}_\mathrm{k,tan} = m_\mathrm{a}^{-1} F_\mathrm{tan}, \qquad v_\mathrm{k,tan}(t_0) = v_\mathrm{k,tan,0} \tag{62}$$

where $\dot{v}_\mathrm{k,tan}$, $v_\mathrm{k,tan}$, and $F_\mathrm{acc,tan} = F_\mathrm{tan}$ are the change of speed (i.e. the acceleration), the speed, and the acceleration force into the tangential direction (in short: tangential force F_tan).

2. Tangential Speed Controller Equations

The speed controller is derived for the plant (62). Herein, $F_\mathrm{tan,set}$ is used as a virtual actuator, i.e. the new set values of the actual three actuations $C_\mathrm{D,rot,set}$, $c_\mathrm{L,set}$, and $C_\mathrm{D,k,a,set}$ generate $F_\mathrm{tan,set}$, but this function $F_\mathrm{tan,set}(C_\mathrm{D,rot,set}, c_\mathrm{L,set}, C_\mathrm{D,k,a,set})$ is inverted by a control allocation in a later step.

Again, simply a P-controller is utilized, i.e.

$$F_\mathrm{tan,set} = G_\mathrm{P,v} \mathit{\Delta} v_\mathrm{k,tan}, \qquad \mathit{\Delta} v_\mathrm{k,tan} = v_\mathrm{k,tan,set} - v_\mathrm{k,tan} \tag{63}$$

with speed error $\mathit{\Delta} v_\mathrm{k,tan}$, speed set value $v_\mathrm{k,tan,set}$, and proportional gain $G_\mathrm{P,v}$.

Figure 3 illustrates the tangential speed control loop. It also illustrates the idea of the tangential force control allocation, which inverts the static nonlinear part of the plant. It is assumed that the control allocation works perfectly, such that the tangential force actuation can be approximated as first order delay with the actuation time constant T_a equal to the highest time constant of the actually involved actuators, $T_\mathrm{a} = \max\{T_{C_\mathrm{D,rot}}, T_{c_\mathrm{L}}, T_{C_\mathrm{D,k,a}}\}$. This assumption can be justified, because the here utilized simple model can indeed be perfectly inverted (for steady-state) and because the highest actuator time constant defines when F_tan is achieved for a set value $F_\mathrm{tan,set}$.

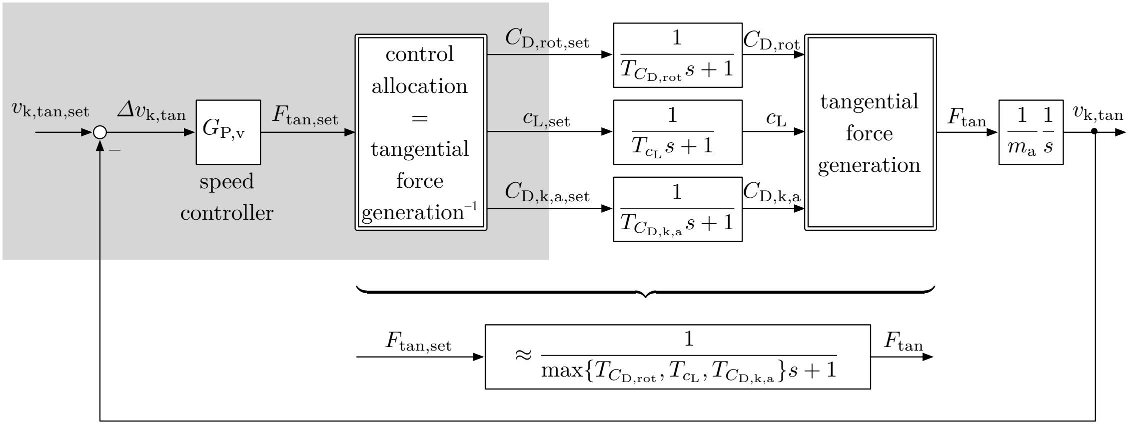

Figure 3 Block diagram of the tangential speed control loop.

3. Controller Parametrization and Stability

In view of Fig. 3 the closed loop transfer function is

$$\frac{v_\mathrm{k,tan}}{v_\mathrm{k,tan,set}} = \frac{1}{\frac{T_\mathrm{a} m_\mathrm{a}}{G_\mathrm{P,v}} s^2 + \frac{m_\mathrm{a}}{G_\mathrm{P,v}} s + 1}. \tag{64}$$

The speed control loop is stable if $G_\mathrm{P,v} > 0$, because then the denominator is a 2nd order Hurwitz polynomial.

Like the temperature control loop in Sect. III.A.3, the speed control loop is parametrized through pole-placement by comparing the denominator of (64) with that of a second order delay (47): The closed speed control loop time constant $T_\# = T_{\mathrm{v},\circ}$ and damping $D_\# = D_{\mathrm{v},\circ}$ are then defined by the two equations

$$T_{\mathrm{v},\circ}^2 = \frac{T_\mathrm{a} m_\mathrm{a}}{G_\mathrm{P,v}}, \tag{65}$$

$$2 D_{\mathrm{v},\circ} T_{\mathrm{v},\circ} = \frac{m_\mathrm{a}}{G_\mathrm{P,v}}. \tag{66}$$

Again, there is only one degree of freedom, $G_{\mathrm{P,v}}$, so the control designer chooses $T_{\mathrm{v},\circ}$ or $D_{\mathrm{v},\circ}$. The latter is used here, for which $G_{\mathrm{P,v}}$ is given by squaring (66), substituting (65), and solving for $G_{\mathrm{P,v}}$,

$$G_{\mathrm{P,v}} = \frac{m_{\mathrm{a}}}{4D_{\mathrm{v},\circ}^{2}T_{\mathrm{a}}}. \tag{67}$$

4. Tangential Speed Set Value

The optimal airflow speed from a steady drag power kite model is given by (cf. [10, Eq. (28.14)])

$$v_{\mathrm{a,opt}} = \frac{2}{3}\cos(\varphi)\cos(\vartheta)v_{\mathrm{w}}\frac{C_{\mathrm{L,n}}}{C_{\mathrm{D,eq,n}}}, \tag{68}$$

where φ and ϑ are the azimuth and elevation angles of the kite w.r.t. the wind velocity (wind speed vector) defined by

$$\varphi = \arctan_2(\boldsymbol{r}_{\mathrm{k}} \bullet \boldsymbol{y}, \boldsymbol{r}_{\mathrm{k}} \bullet \boldsymbol{x}) - \varphi_{\mathrm{w}}, \qquad \vartheta = -\arctan\left[\frac{(\boldsymbol{r}_{\mathrm{k}} - \boldsymbol{r}_{\mathrm{gs}}) \bullet \boldsymbol{z}}{\sqrt{(\boldsymbol{r}_{\mathrm{k}} \bullet \boldsymbol{x})^2 + (\boldsymbol{r}_{\mathrm{k}} \bullet \boldsymbol{y})^2}}\right], \tag{69}$$

and $C_{\mathrm{L,n}}$ and $C_{\mathrm{D,eq,n}}$ are the nominal total lift and equivalent drag coefficients which occur at $c_{\mathrm{L}} = c_{\mathrm{L,n}}$ and $C_{\mathrm{D,k,a}} = C_{\mathrm{D,k,a,min}} = 0$ in (20)–(30). That optimal value $v_{\mathrm{a,opt}}$ is used as the set value of the airflow speed $v_{\mathrm{a,set}}$, but bounded by the minimum and maximum values, i.e.

$$v_{\mathrm{a,set}} = \mathrm{limit}(v_{\mathrm{a,min}}, v_{\mathrm{a,opt}}, v_{\mathrm{a,max}}) \tag{70}$$

where

$$v_{\mathrm{a,max}} = f_{\text{over-v}}v_{\mathrm{a,n}} \tag{71}$$

is the maximum instantaneous airflow speed set value with overloading (or underloading) factor $f_{\text{over-v}}$ and with nominal airflow speed $v_{\mathrm{a,n}}$, and where $v_{\mathrm{a,min}}$ is the minimum airflow speed. The latter two airflow speeds are coupled with the nominal and minimal lift force, respectively, which both occur at the nominal airfoil lift coefficient $c_{\mathrm{L}} = c_{\mathrm{L,n}}$ and at the nominal and minimal airflow speed, respectively, i.e., similar to (55),

$$F_{\mathrm{L,min}} = \frac{1}{2}\rho v_{\mathrm{a,min}}^{2}A\frac{c_{\mathrm{L,n}}}{1+\frac{2}{Æ}} \qquad \Leftrightarrow v_{\mathrm{a,min}} = \sqrt{\frac{F_{\mathrm{L,min}}}{\frac{1}{2}\rho A\frac{c_{\mathrm{L,n}}}{1+\frac{2}{Æ}}}}, \tag{72}$$

$$F_{\mathrm{L,n}} = \frac{1}{2}\rho v_{\mathrm{a,n}}^{2}A\frac{c_{\mathrm{L,n}}}{1+\frac{2}{Æ}} \qquad \Leftrightarrow v_{\mathrm{a,n}} = \sqrt{\frac{F_{\mathrm{L,n}}}{\frac{1}{2}\rho A\frac{c_{\mathrm{L,n}}}{1+\frac{2}{Æ}}}}. \tag{73}$$

From that airflow speed set value (70), the set airflow velocity is

$$\boldsymbol{v}_{\mathrm{a,set}} = v_{\mathrm{a,set}} \operatorname{dir}(\boldsymbol{v}_{\mathrm{a}}) \tag{74}$$

where $\boldsymbol{v}_{\mathrm{a}}$ is the currently measured/identified airflow velocity. The set kite velocity is then given by inverting (14), i.e.

$$\boldsymbol{v}_{\mathrm{k,set}} = \boldsymbol{v}_{\mathrm{w}}(\boldsymbol{r}_{\mathrm{k}}) - \boldsymbol{v}_{\mathrm{a,set}} \tag{75}$$

with the currently measured/identified/estimated wind velocity at the kite $\boldsymbol{v}_{\mathrm{w}}(\boldsymbol{r}_{\mathrm{k}})$. Finally, the tangential kite speed set value is

$$v_{\mathrm{k,tan,set}} = \boldsymbol{v}_{\mathrm{k,set}} \bullet \boldsymbol{e}_{\mathrm{tan}} \tag{76}$$

with the currently measured/identified tangential direction $\boldsymbol{e}_{\mathrm{tan}}$.

D. Tangential Force Control Allocation

As mentioned in the previous section and illustrated in Fig. 3, the tangential force control allocation inverts the tangential force generation, i.e. it computes the actuations $C_{\mathrm{D,rot,set}}$, $c_{\mathrm{L,set}}$, and $C_{\mathrm{D,k,a,set}}$ to achieve a given $F_{\mathrm{tan,set}} = F_{\mathrm{tan}}$ in steady-state. Although it should be possible to find an analytical solution for this inversion and for the here utilized model, a numerical solution is pursued for sake of simplicity as well as for the possibility for its use with minimal changes in a more elaborate and more nonlinear model or real system. However, because the here utilized model is not very nonlinear, the derived numerical solution is exact. In the following, first a few functions are defined for later convenient use, then the proposed algorithm is detailed step by step.

1. Definition of "force"-Function

The "force"-function

$$F_{\mathrm{tan,set}} \leftarrow \mathrm{force}(C_{\mathrm{D,rot,set}}, c_{\mathrm{L,set}}, C_{\mathrm{D,k,a,set}}) \tag{77}$$

computes the (steady-state) tangential force (i.e. the tangential set force) s.t. the currently measured/identified states and s.t. the passed set values $C_{\mathrm{D,rot,set}}$, $c_{\mathrm{L,set}}$, $C_{\mathrm{D,k,a,set}}$, i.e. the equations (25), (22), (11), (30), (29), (28), (27), (26), (24), (21), (12), (10), (4), (3), and

$$F_{\mathrm{tan}} = F_{\mathrm{acc,tan}} = \boldsymbol{F}_{\mathrm{acc}} \bullet \boldsymbol{e}_{\mathrm{tan}} \tag{78}$$

are computed in that order.

2. *Definition of “linpol”-Function*

The “linpol”-function

$$x \leftarrow \operatorname{linpol}\left[y, (x_1, y_1, x_2, y_2)\right] \tag{79}$$

linearly interpolates between two points (x_1, y_1) and (x_2, y_2), and returns the value x for a given y value. If $x_1 = x_2$, “linpol” simply returns $x \leftarrow x_1$.

3. *Definition of “quadpol”-Function*

The “quadpol”-function

$$x \leftarrow \operatorname{quadpol}\left[y, (x_1, y_1, x_2, y_2, x_3, y_3)\right] \tag{80}$$

quadratically interpolates between three points (x_1, y_1), (x_2, y_2), and (x_3, y_3), and returns the value x for a given y value. Note that usually x has two results, which are both returned by “quadpol”. The actual selected value is to be chosen outside “quadpol”, i.e. “quadpol” returns two values. In case $x_1 = x_2$, $x_2 = x_3$, or/and $x_1 = x_3$, “quadpol” falls back to “linpol”,

$$x \leftarrow \begin{cases} \operatorname{linpol}\left[y, (x_1, y_1, x_2, y_2)\right] & \text{for } x_1 = x_3 \text{ or } x_2 = x_3, \\ \operatorname{linpol}\left[y, (x_2, y_2, x_3, y_3)\right] & \text{for } x_1 = x_2 \text{ (or } x_1 = x_3\text{).} \end{cases} \tag{81}$$

4. *Tangential Force Control Allocation Algorithm*

The tangential force control allocation computes the actuations $C_{\mathrm{D,rot,set}}$, $c_{\mathrm{L,set}}$, and $C_{\mathrm{D,k,a,set}}$, such that a given value for $F_{\mathrm{tan,set}}$ is reached (as closely as possible). Initially, all actuations are set to their optimal values resulting from a steady-state drag power kite model (cf. e.g. [10]). Then the actuations are altered from their optimal value to reach the $F_{\mathrm{tan,set}}$ demand in the following order: First $C_{\mathrm{D,rot,set}}$ is utilized until its bounds are reached. If necessary, second $c_{\mathrm{L,set}}$ is reduced from its optimal value. If further necessary, third $C_{\mathrm{D,k,a,set}}$ is increased above zero. That actuator utilization provides the highest power extraction, and even results in reduced lift- and tether forces at high winds with potentially high but less harmful gusts. The complete tangential force control allocation algorithm, which is executed at each discrete time step, reads as follows:

1. Initialization: Assign optimal actuations from a steady drag power kite model solution (cf. e.g. [10]), but limited within their bounds, i.e.

$$C_{\mathrm{D,rot,set}} \leftarrow \mathrm{limit}\left(C_{\mathrm{D,rot,min}}, \frac{1}{2}C_{\mathrm{D,eq,n}}, C_{\mathrm{D,rot,max}}\right), \tag{82}$$

$$c_{\mathrm{L,set}} \leftarrow \mathrm{limit}(c_{\mathrm{L,min}}, c_{\mathrm{L,n}}, c_{\mathrm{L,max}}), \tag{83}$$

$$C_{\mathrm{D,k,a,set}} \leftarrow \mathrm{limit}(C_{\mathrm{D,k,a,min}}, 0, C_{\mathrm{D,k,a,max}}). \tag{84}$$

2. Compute the highest achievable tangential force,

$$F_{\mathrm{tan,set},C_{\mathrm{D,rot,min}}} \leftarrow \mathrm{force}(C_{\mathrm{D,rot,min}}, c_{\mathrm{L,set}}, C_{\mathrm{D,k,a,set}}). \tag{85}$$

   Note that $c_{\mathrm{L,set}}$ and $C_{\mathrm{D,k,a,set}}$ already have the values to support obtaining the highest achievable force.

3. If $F_{\mathrm{tan,set}} > F_{\mathrm{tan,set},C_{\mathrm{D,rot,min}}}$,

   3.1. then

$$C_{\mathrm{D,rot,set}} \leftarrow C_{\mathrm{D,rot,min}}. \tag{86}$$

   A larger tangential force is not achievable, i.e. the tangential speed controller's demand cannot be fully satisfied, because the actuators are saturated. *The algorithm ends here (return).*

   3.2. Otherwise, continue with next step.

4. Compute the lowest achievable tangential force by changing the rotor drag coefficient only,

$$F_{\mathrm{tan,set},C_{\mathrm{D,rot,max}}} \leftarrow \mathrm{force}(C_{\mathrm{D,rot,max}}, c_{\mathrm{L,set}}, C_{\mathrm{D,k,a,set}}). \tag{87}$$

5. If $F_{\mathrm{tan,set},C_{\mathrm{D,rot,max}}} < F_{\mathrm{tan,set}}$,

   5.1. it means that $F_{\mathrm{tan,set}}$ is achievable just by changing the rotor drag coefficient. As from (21), (12), (10), (3), and (78) follows $F_{\mathrm{tan}} = c_0 + c_1 C_{\mathrm{D,rot}}$ with some values c_0 and c_1, the set value is found (exactly) by linear interpolation between the two extrema,

$$C_{\mathrm{D,rot,set}} \leftarrow \mathrm{linpol}\left[F_{\mathrm{tan,set}}, (C_{\mathrm{D,rot,max}}, F_{\mathrm{tan,set},C_{\mathrm{D,rot,max}}}, C_{\mathrm{D,rot,min}}, F_{\mathrm{tan,set},C_{\mathrm{D,rot,min}}})\right]. \tag{88}$$

   The algorithm ends here (return).

5.2. Otherwise, it means that $F_{\mathrm{tan,set}}$ is not achievable by changing the rotor drag coefficient alone. It must be set to the maximum

$$C_{\mathrm{D,rot,set}} \leftarrow C_{\mathrm{D,rot,max}}, \tag{89}$$

but also further actuation(s) have to be altered.

6. Compute the lowest achievable tangential force by changing additionally the airfoil lift coefficient,

$$F_{\mathrm{tan,set},c_{\mathrm{L,min}}} \leftarrow \mathrm{force}(C_{\mathrm{D,rot,set}}, c_{\mathrm{L,min}}, C_{\mathrm{D,k,a,set}}). \tag{90}$$

7. If $F_{\mathrm{tan,set},c_{\mathrm{L,min}}} < F_{\mathrm{tan,set}}$,

7.1. it means that $F_{\mathrm{tan,set}}$ is achievable just by changing additionally the airfoil lift coefficient. As from (25), (22), (11), (28), (30), (27), (26), (24), (21), (12), (10), (3), and (78) follows $F_{\mathrm{tan}} = c_0 + c_1 c_{\mathrm{L}} + c_2 c_{\mathrm{L}}^2$ with some values c_0, c_1, and c_2, the set value is found (exactly) by quadratic interpolation. For that, three points are required. A first point is the previously computed one at $c_{\mathrm{L,min}}$. A second point is at $c_{\mathrm{L,n}} = c_{\mathrm{L,max}}$, whose force is also already known from

$$F_{\mathrm{tan,set},c_{\mathrm{L,max}}} = F_{\mathrm{tan,set},C_{\mathrm{D,rot,max}}}. \tag{91}$$

A third point is computed in-between with

$$c_{\mathrm{L,mid}} \leftarrow \frac{c_{\mathrm{L,min}} + c_{\mathrm{L,max}}}{2} \tag{92}$$

by

$$F_{\mathrm{tan,set},c_{\mathrm{L,mid}}} \leftarrow \mathrm{force}(C_{\mathrm{D,rot,set}}, c_{\mathrm{L,mid}}, C_{\mathrm{D,k,a,set}}). \tag{93}$$

The airfoil lift coefficient set value is then

$$c_{\mathrm{L,set}} \leftarrow \mathrm{quadpol}\left[F_{\mathrm{tan,set}}, (c_{\mathrm{L,min}}, F_{\mathrm{tan,set},c_{\mathrm{L,min}}}, c_{\mathrm{L,mid}}, F_{\mathrm{tan,set},c_{\mathrm{L,mid}}}, c_{\mathrm{L,max}}, F_{\mathrm{tan,set},c_{\mathrm{L,max}}})\right]. \tag{94}$$

There are two $c_{\mathrm{L,set}}$ values from "quadpol". The one is chosen which is within the interval $[c_{\mathrm{L,min}}, c_{\mathrm{L,max}}]$ (and possibly closer to $c_{\mathrm{L,max}}$). *The algorithm ends here (return).*

7.2. Otherwise, it means that $F_{\text{tan,set}}$ is not achievable by changing only the rotor drag coefficient and the airfoil lift coefficient. The latter must be set to the minimum

$$c_{\text{L,set}} \leftarrow c_{\text{L,min}}, \tag{95}$$

but also further actuation(s) have to be altered.

8. Compute the lowest achievable tangential force by changing additionally the actuated drag coefficient,

$$F_{\text{tan,set},C_{\text{D,k,a,max}}} \leftarrow \text{force}(C_{\text{D,rot,set}}, c_{\text{L,set}}, C_{\text{D,k,a,max}}). \tag{96}$$

9. If $F_{\text{tan,set},C_{\text{D,rot,max}}} < F_{\text{tan,set}}$,

9.1. it means that $F_{\text{tan,set}}$ is achievable just by changing additionally the actuated drag coefficient. As from (24), (21), (12), (10), (3), and (78) follows $F_{\text{tan}} = c_0 + c_1 C_{\text{D,k,a}}$ with some values c_0 and c_1, the set value is found (exactly) by linear interpolation between the two extrema,

$$C_{\text{D,k,a,set}} \leftarrow \text{linpol}\left[F_{\text{tan,set}}, (C_{\text{D,k,a,min}}, F_{\text{tan,set},C_{\text{D,k,a,min}}}, C_{\text{D,k,a,max}}, F_{\text{tan,set},C_{\text{D,k,a,max}}})\right], \tag{97}$$

where the force at $C_{\text{D,k,a,min}}$ is already known from

$$F_{\text{tan,set},C_{\text{D,k,a,min}}} = F_{\text{tan,set},c_{\text{L,min}}}. \tag{98}$$

The algorithm ends here (return).

9.2. Otherwise, it means that $F_{\text{tan,set}}$ is also not achievable with the highest actuated drag coefficient. It must be set to the maximum

$$C_{\text{D,k,a,set}} \leftarrow C_{\text{D,k,a,max}}. \tag{99}$$

A lower tangential force is not achievable, i.e. the tangential speed controller's demand cannot be fully satisfied, because the actuators are saturated. *The algorithm ends here (return).*

IV. Implementation and Parameters

A. Simulation Execution

The model and control scheme are implemented as a MATLAB-function which computes the time derivatives of all states. Those are then integrated using the forward Euler method. The simulation is stopped when the trajectory is settled, i.e. when the kite flew the maximum number of path loops. With appropriate initial values (particularly of kite position, velocity, and powertrain temperature), the maximum number of path loops can be relatively low. From the last path loop, the mean, minimum, and maximum of important values (e.g. power, force, speed) are computed, which may then be used as a data point in a power curve plot.

B. Tether Spring-Damper Parameters

The tether spring-damper constants are not chosen based on e.g. material properties, because (i) it is hard to estimate the actual values for the compound tether, (ii) a real tether has a mass and a sag and thus effectively has a higher damping and lower spring constant as one would expect from the pure material properties, and (iii) if high spring and damper constants are chosen, a low time step for the integration is required for numerical stability leading to a high computational load. Instead the spring and damper constants are set based on the analysis in Appendix A.

C. Initial Position and Initial Velocity

Instead of specifying the initial position $\boldsymbol{r}_{\mathrm{k},0}$ and initial velocity $\boldsymbol{v}_{\mathrm{k},0}$ directly, they are computed from initial azimuth φ_0, initial elevation ϑ_0, and initial kite speed $v_{\mathrm{k},0}$ by taking into account that the kite essentially can only move on the sphere spanned by the tether:

$$\boldsymbol{v}_{\mathrm{k},0} = \boldsymbol{R}_{\mathrm{z}}(\varphi_0 + \varphi_{\mathrm{w}})\boldsymbol{R}_{\mathrm{y}}(\vartheta_0)\,(0, 0, v_{\mathrm{k},0})^{\top}, \tag{100}$$

$$\boldsymbol{r}_{\mathrm{k},0} = \boldsymbol{R}_{\mathrm{z}}(\varphi_0 + \varphi_{\mathrm{w}})\boldsymbol{R}_{\mathrm{y}}(\vartheta_0)\,(L_{\mathrm{te}}, 0, 0)^{\top} + \boldsymbol{r}_{\mathrm{gs}}. \tag{101}$$

D. Parameter Values to Simulate the Makani Wing 7

The derived model and control scheme are applied for the Makani Wing 7. The model parameters are taken from [10, 41], from the results of a steady model similar to [10, 28, 29], and from estimations (e.g. actuator time constants). Table 1 lists all relevant parameters. Note that a main goal of using the Makani Wing 7 parameters as example is to validate the model against the power curve measurement from [10, Fig. 28.12].

Table 1 Parameters for simulations (Makani Wing 7).

Parameter	Value	Comment/Justification
Implementation parameters.		
integration time	= 0.01 s	good trade-off between accuracy and computational load
max. path loops	= 3	enough to (approximately) settle flight trajectory
Environmental parameters.		

g	$= 9.81\,\mathrm{m/s^2}$	$\approx$ Standard Gravity; but actual value of [10] could differ slightly
ρ	$= 1.255\,\mathrm{kg/m^3}$	standard atmosphere at 15 °C; but actual value of [10] could differ
h_{ref}	$= 30\,\mathrm{m}$	could be anything $\neq 0$ as no wind shear considered in [10] implying $\alpha_{\mathrm{H}} = 0$
α_{H}	$= 0$	no wind shear considered in [10]
$v_{\mathrm{w},h_{\mathrm{ref}}}$	$= 0 \ldots 12\,\mathrm{m/s}$	considered values in [10, Fig. 28.12]
φ_{w}	$= 0$	any value would be valid
τ'_{∞}	$= 0$	ambient temperature is nominal ambient temperature
Kite parameters.		
b	$= 8\,\mathrm{m}$	Ref. [10, Fig. 28.7]
A	$= 3.96\,\mathrm{m}$	Ref. [10, Fig. 28.7]
AR	$= 16.1616$	$= b^2/A$ with $b = 8\,\mathrm{m}$ from [10, Fig. 28.7]
$c_{\mathrm{D,0}}$	$= 0.010$	Ref. [29]
$c_{\mathrm{D,2}}$	$= 0.005$	Ref. [29]
$c_{\mathrm{L,n}}$	$= 2.2475$	$= C_{\mathrm{L,n}}(1 + 2/\mathit{AR})$ with $C_{\mathrm{L,n}} = 2$ from [10, Fig. 28.7]
$c_{\mathrm{L,min\text{-}op}}$	$= 0.5$	estimated
e	$= 0.8$	estimated, slightly higher than $e \approx 0.7$ for rectangular wings to account for the winglets of Wing 7 [10, Fig. 28.7]; but actual value could differ
$C_{\mathrm{D,k,o}}$	$= 0.025$	$= (C_{\mathrm{D,k}} - C_{\mathrm{D,k,mw,i}})_{\mathrm{n}} - (c_{\mathrm{D,0}} + c_{\mathrm{D,0}} c^2_{\mathrm{L,n}})$ with $(C_{\mathrm{D,k}} - C_{\mathrm{D,k,mw,i}})_{\mathrm{n}} = 0.06$ from [10, Table 28.1], cf. (21)–(30)
$C_{\mathrm{D,k,a,max}}$	$= 0.5$	estimated
m_{a}	$= 68\,\mathrm{kg}$	estimated from 60 kg kite mass [41] plus half of the tether mass 16 kg [41]
Tether parameters.		
L_{te}	$= 144\,\mathrm{m}$	Ref. [41]
$c_{\mathrm{D,te}}$	$= 1$	estimated, $\approx c_{\mathrm{D}}$ of cylinder at reasonable Reynolds number
d_{te}	$= 1.1\,\mathrm{cm}$	estimated based on data from [41] and a tether model similar to [8]
$\mathit{\Delta} r'_{\mathrm{te,n}}$	$= 0.001$	estimated (and is large enough for numerical stability)
D_{te}	$= 1$	estimated (critical damping)

Powertrain parameters.		
$P_{\mathrm{a},+,\mathrm{n}}$	$= 20\,\mathrm{kW}$	Ref. [10, Fig. 28.7]
$P_{\mathrm{a},-,\mathrm{n}}$	$= -20\,\mathrm{kW}$	same magnitude as $P_{\mathrm{a},+,\mathrm{n}}$
T_{τ}	$= 30\,\mathrm{s}$	estimated, typical time constant for electrical machine
Ground station parameters.		
$\boldsymbol{r}_{\mathrm{gs}}$	$= (0, 0, 15\,\mathrm{m})$	estimated from [10, Fig. 28.8], but has no effect on power curve as no wind shear considered in [10]
Parameters of remaining actuators.		
$v_{\mathrm{a,min}}$	$= 30.5\,\mathrm{m/s}$	Ref. [10, p. 487]
$v_{\mathrm{a,n}}$	$= 37\,\mathrm{m/s}$	estimated based on model results of a steady model similar to [28, 29]
$F_{\mathrm{L,n}}$	$= 6.8\,\mathrm{kN}$	results from magnitude of (11) with nominal values inserted
$\psi_{\max} = -\psi_{\min}$	$= 30\,^{\circ}$	estimated
$T_{C_{\mathrm{D,rot}}}$	$= 0.2\,\mathrm{s}$	estimated (for closed rotor speed control loop)
$T_{c_{\mathrm{L}}} = T_{C_{\mathrm{D,k,a}}}$	$= 0.1\,\mathrm{s}$	estimated (for control surfaces)
T_{ψ}	$= 0.2\,\mathrm{s}$	estimated (for closed roll control loop)
Controller parameters.		
$f_{\text{over-P}}$	$= 2$	estimated feasible (and required)
$f_{\text{over-F}}$	$= 1$	no force overloading (or underloading) considered
$f_{\text{over-v}}$	$= 1$	no speed overloading (or underloading) considered
$D_{\tau,\circ}$	$= 1$	critical damping chosen
$D_{\mathrm{v},\circ}$	$= 1$	critical damping chosen
Initial values.		
φ_0	$= 30\,^{\circ}$	for fast settling
ϑ_0	$= -30\,^{\circ}$	for fast settling
$v_{\mathrm{k},0}$	$= v_{\mathrm{a,n}}$	for fast settling (note that $v_{\mathrm{k}} \approx v_{\mathrm{a}}$)
$C_{\mathrm{D,rot},0}$	$= C_{\mathrm{D,eq,n}}/2$	for most wind speeds close to the final value

$c_{\mathrm{L},0}$	$= c_{\mathrm{L,n}}$	for most wind speeds close to the final value
$C_{\mathrm{D,k,a},0}$	$= 0$	for most wind speeds close to the final value
ψ_0	$= 0$	no roll at beginning
τ'_0	$= 1$	for fast settling at high wind speeds; at low wind speeds, temperature likely drops fast and power is not constrained by the temperature

V. Simulation Results and Model Validation with Measurements from the Makani Wing 7

In the following, simulation results with parameters of the Makani Wing 7 are reported and discussed in detail. The results are also used to validate the derived model against the measurements reported in [10].

A. Power Curve Results

The most important question here is how the simulated power curve compares with that of the steady model [10, 28, 29] and with measurements [10]. Figure 4 shows the results from this paper's model with mean values over a flight path loop plotted in solid, and the range of minimum and maximum values over a flight path loop plotted as area. Those results are compared to a steady model similar to [10, 28, 29] plotted in dashed. The vertical dashed lines indicate the different power curve regions, cf. [28, 29].

It can be seen that the majority of the mean values over a flight path loop match well with those of the steady model. In particular, the most important one, the mean aerodynamic power, is almost identical to that of the steady model.

B. Power Curve: Steady Model vs. Point-Mass Model vs. Reality

Figure 5 shows an overlay of (i) [10, Fig. 28.12], which contains measured powers and simulation results of Makani/Vander Lind, and (ii) Fig. 4 (row 1), with size, axes, and line thickness altered for better perception. It can be seen that the resulting mean power of the model and controller of this paper is close to the other simulation results as well as measurements conducted by Makani/Vander Lind. The slightly lower power of the model and controller of this paper can be explained by (i) the non-zero mean azimuth angle assumed in the steady model (cf. [10]), while in fact the recorded mean of the absolute values is $\approx 10\,^{\circ}$, see last row in Fig. 4, and by (ii) the non-optimized flight path e.g. with Maximum Power Point (MPP) Tracking. In fact, slightly changing the flight path results almost exactly in the power curve of Makani's/Vander Lind's results. It should be noted that an MPP-tracker might not only optimize the flight path, but also the airflow speed set value or the rotor drag coefficient as function of the position within the trajectory.

C. Flight Trajectories over Wind Speeds

Figure 6 shows the flight trajectories at different wind speeds. The start and end points of all trajectories are almost

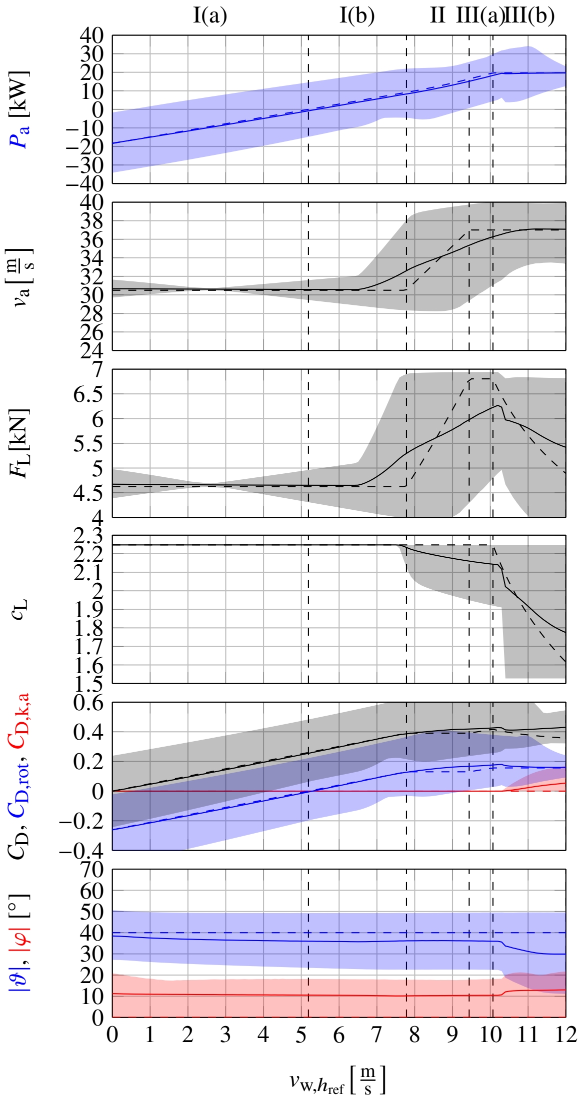

Figure 4 **Power curve simulation results.**

identical, which indicates that the trajectory is settled, even-though the shown trajectories are just the third path loop (cf. Table 1). Apart from the trajectory at $v_{w,h_{ref}} = 12\,m/s$, each one is almost a circle (clockwise) with the center point at about $(\varphi, \vartheta) = (0\,°, -40\,°)$. However, the circle is not very smooth, which is caused by the switching behavior of the target point tracking-based flight path controller. This indicates again space for optimizations.

The flight trajectory at $v_{w,h_{ref}} = 12\,m/s$ deviates rather significantly from others: When the kite flies downwards, the potential energy increases the airflow speed which is controlled and limited by the tangential speed controller and the tangential force control allocation, which in turn reduces the airfoil lift coefficient, visible in Fig. 4. A reduced airfoil lift coefficient reduces the maximum centripetal force and therefore the instantaneous flight path turning radius becomes larger. This effect is much weaker or non existent when the kite flies upwards. As a result of flying circles, here the kite reaches dangerously low altitudes which should of course be targeted in improvements of the flight path controller.

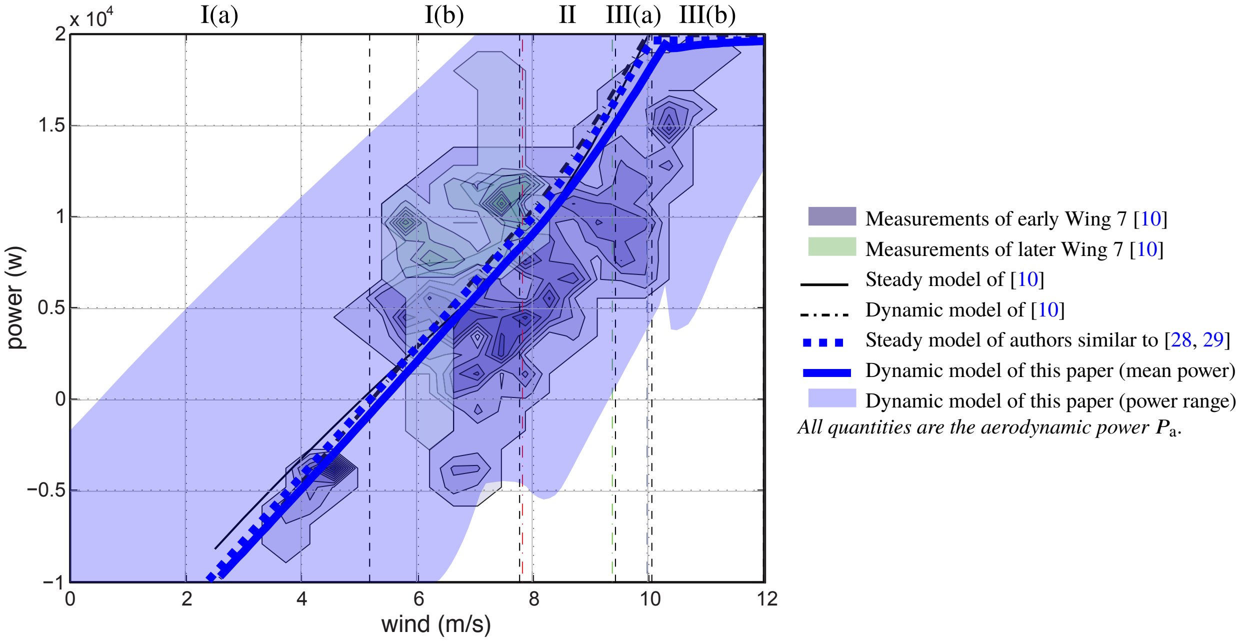

All quantities are the aerodynamic power P_a.

Figure 5 Comparison of power curves from different models and measurements.

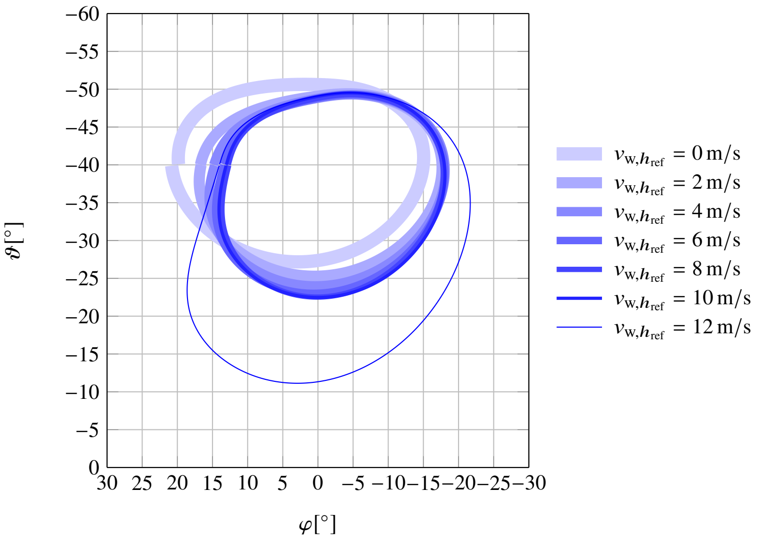

Figure 6 Flight trajectories at different wind speeds.

Alternatively, to circumvent too low altitudes, Makani proposes to use the vertical wings and sideslipping as additional actuation to generate an additional centripetal force contribution, patented in [42].

D. Time Course of Important Values

To detail the proper working of the control method, the time course of important values are reviewed at $v_{w,h_{ref}} = 10\,m/s$ for the third flight path loop. Figure 7 gives the results.

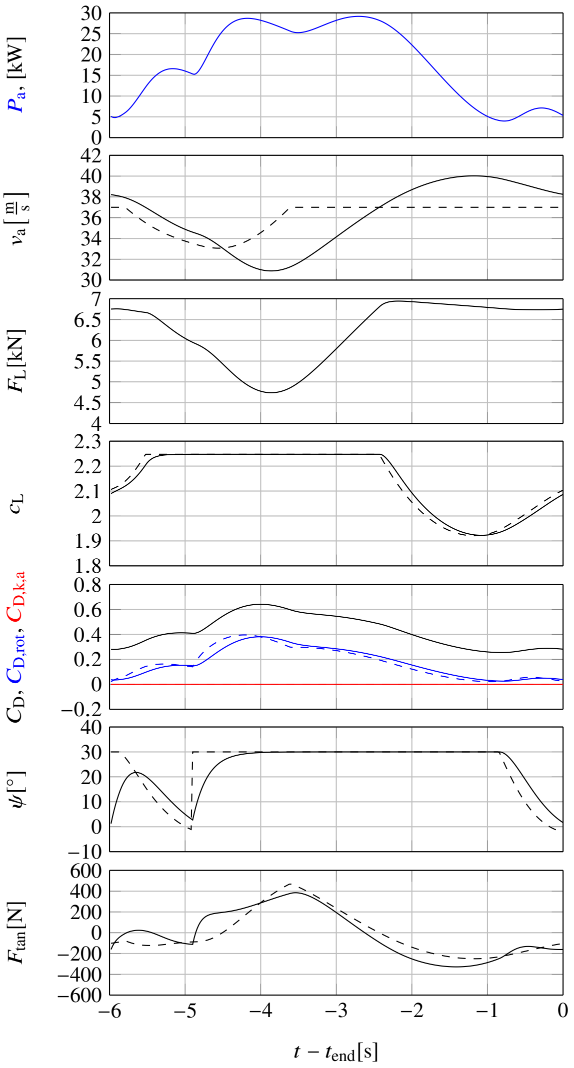

Figure 7 Time course of important values at 10 m/s wind speed with limited set values in dashed and actual values in solid.

A path loop takes almost exactly 6 s. The power oscillates significantly: When the kite flies downwards the nominal power is exceeded (overloading) while the power is well below its nominal value when the kite flies upwards. The airflow speed can be tracked, but with a visible control error, explainable by the tangential speed P-controller and its critical dimensioning. However, with a more aggressive gain or a PI-controller, the tangential force control allocation might reduce the airfoil lift and increase the actuated drag earlier and more often and thus may reduce the mean power. This is obviously a trade-off between control accuracy and the dimensioning of the plant with enough overloading capability or safety factors. Nevertheless, the important lift force hardly exceeds its nominal value, also visible in Fig. 4. Thus, exceeded airflow speeds can be tolerated. The proper working of the tangential force control allocation is visible in the last row of Fig. 7, showing a good match of the set values and actual values. The kite's roll angle is almost all the time at its maximum positive value. Due to gravity, it also has to be reduced for some time to regain altitude. Here, the switching behavior of the flight path controller is visible and affects most other values, cf. e.g. Fig. 7 at $t - t_{\mathrm{end}} \approx -5\,\mathrm{s}$.

E. Dynamic Change of Wind Speed

To further demonstrate the proper working of the control scheme, it is challenged with a wind speed step change from $v_{\mathrm{w},h_{\mathrm{ref}}} = 10\,\mathrm{m/s}$ to $v_{\mathrm{w},h_{\mathrm{ref}}} = 6\,\mathrm{m/s}$ after the first path loop (i.e. when the kite flies upward). Note that such a stepwise change is unlikely in reality, but constitutes an excellent challenge for the control scheme. If the control scheme is successful in suppressing such a disturbance, it will less likely have problems in realistic wind conditions. Figure 8 (left) reports the results.

As expected, the rotor drag is reduced and so are the power and airflow speed. For a short time between $t = 8 \ldots 10\,\mathrm{s}$ the rotors are used as propellers in motor mode. The new set values are reached within less than a second. The step change is even hardly visible in the tangential force values, cf. last row in Fig. 8 (left).

F. Dynamic Change of Powertrain Temperature Set Value

As one further challenge for the control scheme, the per unit set temperature of the powertrain is changed stepwise from $\tau'_{\mathrm{set}} = 1.0$ to $\tau'_{\mathrm{set}} = 0.8$ after the first path loop. Note again that such a stepwise change of τ'_{set} is unrealistic or has no practical meaning, but constitutes another excellent challenge for the controller. Figure 8 (right) reports the results.

The limitation controller brings the power down to zero almost immediately after the step change of τ'_{set} for about 6 s to cool down the powertrain quickly. The now missing tangential force actuated with $C_{\mathrm{D,rot}}$ is simply substituted by $C_{\mathrm{D,k,a}}$, automatically by the proposed control allocation. The rather long time in which the power is zero is hardly visible in the tangential force [last row of Fig. 8 (right)] or in the airflow speed [third row of Fig. 8 (right)]. This indicates that the tangential force control allocation works as expected.

G. Results for Figure Eight Flight Paths

The Makani systems are flown in circles. To not twist the tether while allowing an infinite number of circle loops, a rather complex gimbal system and slip rings are required for the ground station tether connection. To avoid that complexity (which is additionally in part patented by Makani and thus usage might be restricted), figure eight paths are also tested. This allows yet another test for the proposed control scheme, namely to control the kite for different flight paths. Figure 9 shows the kite's trajectory for an inside-down and inside-up figure eight.

The control scheme stabilizes the kite's trajectory well. However, the inside-up figure eight looks quite distorted. This can be explained by the not-insignificant gravitational force which acts as centrifugal force for a longer time of the turns than it acts as centripetal force. Moreover, when the kite flies downwards, again the lift coefficient is reduced

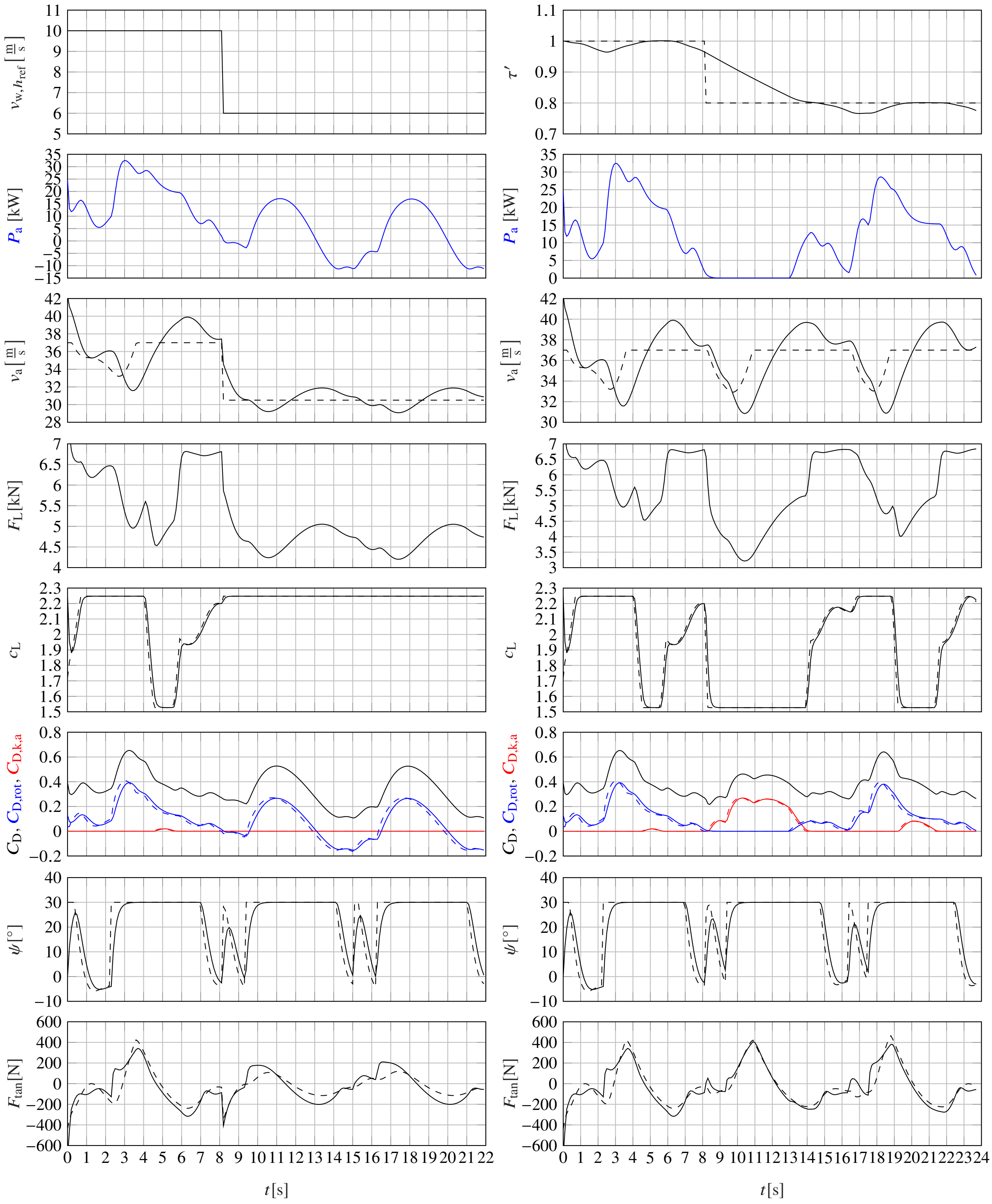

Figure 8 Time course of important values with limited set values in dashed and actual values in solid. Left: step of 10 m/s wind speed to 6 m/s after the first path loop. Right: with 10 m/s wind speed and step of per unit temperature set value of 1.0 to 0.8 after the first path loop.

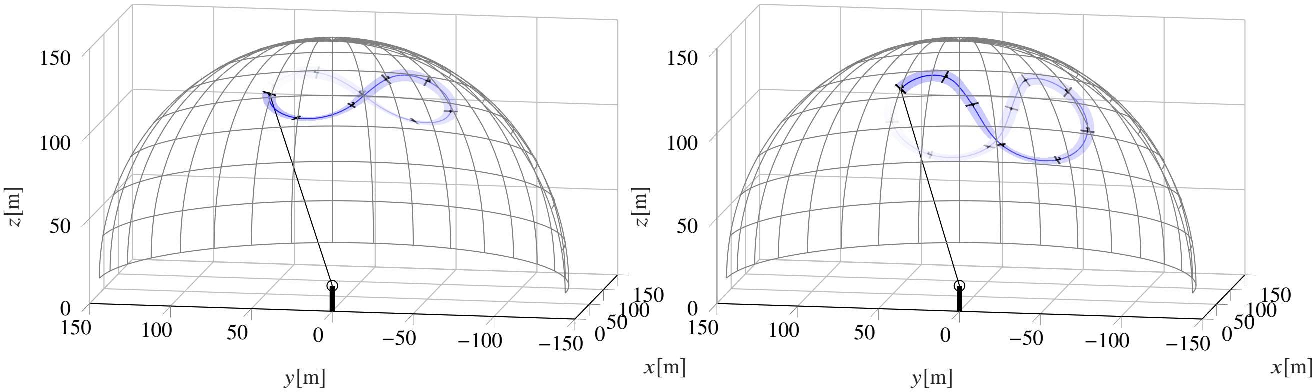

Figure 9 Inside-down (left) and inside-up (right) figure eight trajectories at 10 m/s wind speed with the kite's orientation every 1 s before the path loop ends.

which additionally reduces the maximum actuatable centripetal force. Both is exactly opposite for the inside-down figure eight path, which is an almost perfect eight.

VI. Conclusions

This paper proposes a control scheme to control a drag power kite over the entire wind speed range. The complete control scheme is based on conventional P-controllers and parts to allocate actuations as well as to invert nonlinearities, i.e. control allocations. The control scheme includes a temperature controller and the possibility to overload the powertrain temporarily. Satisfying temperature-, power-, force-, speed-, and actuator constraints are an integral part. Another key part of the control scheme is the proposed tangential force control allocation. Simulation results indicate the proper working of the control scheme. Moreover, the recorded power curve matches well with steady models from both the authors and Makani as well as with the measurements recorded by Makani. The temporary overloading of the powertrain with about twice the nominal power can be concluded as a requirement, otherwise the mean power would be significantly lower. An overloading or underloading of the forces and speeds are not required. Due to the reduction of the lift coefficient and thus reduction of the maximum centripetal force at high wind speeds, one can conclude that the inside-down figure eight flight path is the best alternative compared to other patterns.

It must be highlighted, that (i) all controllers are only P-controllers, (ii) the flight path controller is based on simple target point switching, and (iii) there is no MPP-Tracking or other means of real time optimization considered (apart from using the optimal solution of the airflow speed from a steady model as airflow speed set value).—Yet, the control scheme stabilizes the kite well, a good or the expected amount of power is generated, the limits are satisfied, and thus the control problem is solved well. This is because the P-controllers are applied for control-oriented plant submodels and the nonlinear parts are canceled out (or linearized) by control allocations. Therefore, the control scheme has a rather low complexity and is rather cheap in terms of computational costs.

Nevertheless, steady-state errors cannot be excluded with P-controllers, particularly also in a real system in which the dynamics, parameters, and states are not exactly available. PI-controllers may improve the control performance, but do also require anti-wind-up, which increases complexity. Optimizations to the control scheme should be targeted in future research. Moreover, the simple models for actuators and aerodynamics should be replaced by more sophisticated ones and finally the control scheme should be tested on a real drag power kite plant for further validation.

Appendix

A. Derivation of Useful Tether Spring-Damper Parameters

The kite's (or point-mass's) dynamics into the radial (or tether) direction is given by

$$m_\mathrm{a}\ddot{r}_\mathrm{k,r} = F_\mathrm{acc,r} + F_\mathrm{iner,r}, \tag{102}$$

where $F_\mathrm{iner,r}$ denotes inertial forces into the $\boldsymbol{e}_\mathrm{r}$-direction (initial conditions are dropped for sake of brevity).

Substituting (5) into (9) under the conditions $\mathit{\Delta} r_\mathrm{te} > 0$ and $F_\mathrm{te,sd} > 0$, substituting that further into (3) and dot-multiply with $\boldsymbol{e}_\mathrm{r}$, gives the acceleration force in the radial direction

$$F_\mathrm{acc,r} = F_\mathrm{g,r} + F_\mathrm{a,r} - \varsigma_\mathrm{te}\mathit{\Delta} r_\mathrm{te} + \xi_\mathrm{te}\mathit{\Delta} v_\mathrm{te}, \tag{103}$$

where $F_\mathrm{g,r}$ and $F_\mathrm{a,r}$ are the gravitational and aerodynamic forces in the $\boldsymbol{e}_\mathrm{r}$-direction. Substituting that into (102) gives

$$m_\mathrm{a}\ddot{r}_\mathrm{k,r} = F_\mathrm{g,r} + F_\mathrm{a,r} - \varsigma_\mathrm{te}\mathit{\Delta} r_\mathrm{te} + \xi_\mathrm{te}\mathit{\Delta} v_\mathrm{te} + F_\mathrm{iner,r}. \tag{104}$$

As by definition

$$\mathit{\Delta} v_\mathrm{te} = \frac{\mathrm{d}}{\mathrm{d}t}\mathit{\Delta} r_\mathrm{te} = \dot{r}_\mathrm{k,r}, \qquad \frac{\mathrm{d}}{\mathrm{d}t}\mathit{\Delta} v_\mathrm{te} = \frac{\mathrm{d}^2}{\mathrm{d}t^2}\mathit{\Delta} r_\mathrm{te} = \ddot{r}_\mathrm{k,r}, \tag{105}$$

Eq. (104) becomes

$$m_\mathrm{a}\frac{\mathrm{d}^2}{\mathrm{d}t^2}\mathit{\Delta} r_\mathrm{te} = -\varsigma_\mathrm{te}\mathit{\Delta} r_\mathrm{te} - \xi_\mathrm{te}\frac{\mathrm{d}}{\mathrm{d}t}\mathit{\Delta} r_\mathrm{te} + \underbrace{F_\mathrm{g,r} + F_\mathrm{a,r} + F_\mathrm{iner,r}}_{=:F_\mathrm{dist,r}}, \tag{106}$$

in which $F_\mathrm{dist,r}$ is summarized as disturbance or excitation term/force. Eq. (106) solved for $\mathit{\Delta} r_\mathrm{te}$ reads in the Laplace-domain

$$\mathit{\Delta} r_\mathrm{te} = \frac{\frac{1}{\varsigma_\mathrm{te}}}{\frac{m_\mathrm{a}}{\varsigma_\mathrm{te}}s^2 + \frac{\xi_\mathrm{te}}{\varsigma_\mathrm{te}}s + 1}F_\mathrm{dist,r}. \tag{107}$$

Comparing the denominator with that of a second order delay (47), the time constant $T_{\#} = T_{\mathrm{te}}$ and damping $D_{\#} = D_{\mathrm{te}}$ are defined by

$$T_{\mathrm{te}}^2 = \frac{m_{\mathrm{a}}}{\varsigma_{\mathrm{te}}}, \tag{108}$$

$$2 D_{\mathrm{te}} T_{\mathrm{te}} = \frac{\xi_{\mathrm{te}}}{\varsigma_{\mathrm{te}}}. \tag{109}$$

Moreover, the elongation $\Delta r_{\mathrm{te}} / L_{\mathrm{te}}$ at steady-state $s = 0$ and in per unit is given by

$$\Delta r_{\mathrm{te}}(s = 0) = \frac{\frac{1}{\varsigma_{\mathrm{te}}}}{\frac{m_{\mathrm{a}}}{\varsigma_{\mathrm{te}}} 0^2 + \frac{\xi_{\mathrm{te}}}{\varsigma_{\mathrm{te}}} 0 + 1} F_{\mathrm{dist,r}} \quad | : L_{\mathrm{te}} \qquad \Leftrightarrow \Delta r'_{\mathrm{te},0} := \frac{\Delta r_{\mathrm{te}}}{L_{\mathrm{te}}}(s = 0) = \frac{F_{\mathrm{dist,r}}}{\varsigma_{\mathrm{te}} L_{\mathrm{te}}}, \tag{110}$$

where $\Delta r'_{\mathrm{te},0}$ is the per unit steady-state elongation.

Usually, a good estimate tends to be available for the per unit elongation at the nominal forces $\Delta r'_{\mathrm{te,n}}$ (which is rather low) and for the damping D_{te} (which is about the critical value one). With the simplified nominal force in the tether direction $F_{\mathrm{dist,r}} \approx F_{\mathrm{L,n}}$ in (110), the spring constant is

$$\Delta r'_{\mathrm{te,n}} = \frac{F_{\mathrm{L,n}}}{\varsigma_{\mathrm{te}} L_{\mathrm{te}}} \qquad \Leftrightarrow \varsigma_{\mathrm{te}} = \frac{F_{\mathrm{L,n}}}{\Delta r'_{\mathrm{te,n}} L_{\mathrm{te}}}, \tag{111}$$

and the damper constant is given by squaring (109), substituting (108) and (111), and rearranging

$$\xi_{\mathrm{te}} = 2 D_{\mathrm{te}} \sqrt{\frac{m_{\mathrm{a}} F_{\mathrm{L,n}}}{\Delta r'_{\mathrm{te,n}} L_{\mathrm{te}}}}. \tag{112}$$

The time constant (108) then becomes

$$T_{\mathrm{te}} = \sqrt{\frac{m_{\mathrm{a}} \Delta r'_{\mathrm{te,n}} L_{\mathrm{te}}}{F_{\mathrm{L,n}}}}, \tag{113}$$

which is a measure for the upper limit for the time step of the numerical integration of the system of nonlinear ordinary differential equations to avoid numerical instability.

Acknowledgments

The authors would like to thank Christoph Hackl for his proofreading and feedback.

References

[1] Loyd, M., “Crosswind kite power (for large-scale wind power production),” *Journal of Energy*, Vol. 4, No. 3, 1980, pp. 106–111. doi:10.2514/3.48021.

[2] Ahrens, U., Diehl, M., and Schmehl, R. (eds.), *Airborne Wind Energy*, Green Energy and Technology, Springer Berlin Heidelberg, 2013. doi:10.1007/978-3-642-39965-7.

[3] Fagiano, L., and Milanese, M., "Airborne Wind Energy: An overview," *American Control Conference (ACC)*, 2012, pp. 3132–3143. doi:10.1109/ACC.2012.6314801.

[4] "Airborne Wind Energy Systems: A review of the technologies," *Renewable and Sustainable Energy Reviews*, Vol. 51, 2015, pp. 1461 – 1476. doi:10.1016/j.rser.2015.07.053.

[5] Schmehl, R. (ed.), *Airborne Wind Energy*, Green Energy and Technology, Springer, Singapore, 2018. doi:10.1007/978-981-10-1947-0.

[6] Mendonça, A. K. d. S., Vaz, C. R., Lezana, A. G. R., Anacleto, C. A., and Paladini, E. P., "Comparing Patent and Scientific Literature in Airborne Wind Energy," *Sustainability*, Vol. 9, No. 6, 2017. doi:10.3390/su9060915.

[7] Kolar, J., Friedli, T., Krismer, F., Looser, A., Schweizer, M., Steimer, P., and Bevirt, J., "Conceptualization and multi-objective optimization of the electric system of an Airborne Wind Turbine," *2011 IEEE International Symposium on Industrial Electronics*, 2011, pp. 32–55. doi:10.1109/ISIE.2011.5984131.

[8] Bauer, F., and Kennel, R. M., "Fault Tolerant Power Electronic System for Drag Power Kites," *Journal of Renewable Energy (Hindawi)*, Vol. 2018, 2018. doi:10.1155/2018/1306750.

[9] X Development LLC, "Makani," , 2017. URL https://x.company/makani/.

[10] Vander Lind, D., *Analysis and Flight Test Validation of High Performance Airborne Wind Turbines*, Springer Berlin Heidelberg, Berlin, Heidelberg, 2013, pp. 473–490. doi:10.1007/978-3-642-39965-$7_2$8.

[11] Lind, D. V., "Developing a 600 kW Airborne Wind Turbine," *Book of Abstracts of the International Airborne Wind Energy Conference 2015*, edited by R. Schmehl, Delft University of Technology, Delft, The Netherlands, 2015, pp. 14–17. doi:10.4233/uuid:7df59b79-2c6b-4e30-bd58-8454f493bb09.

[12] Felker, F., "Progress and Challenges in Airborne Wind Energy," *Book of Abstracts of the Airborne Wind Energy Conference 2017*, edited by M. Diehl, R. Leuthold, and R. Schmehl, Albert Ludwigs University of Freiburg and Delft University of Technology, Freiburg, Germany, 2017, p. 13. doi:10.4233/uuid:4c361ef1-d2d2-4d14-9868-16541f60edc7.

[13] Wijnja, J., Schmehl, R., De Breuker, R., Jensen, K., and Vander Lind, D., "Aeroelastic Analysis of a Large Airborne Wind Turbine," *Journal of Guidance, Control, and Dynamics*, 2018. doi:10.2514/1.G001663.

[14] Diehl, M., "Real-time optimization for large scale nonlinear processes," Dissertation, Ruprecht-Karls-Universität Heidelberg, 2001. doi:10.11588/heidok.00001659.

[15] Houska, B., and Diehl, M., "Optimal Control of Towing Kites," *Proceedings of the 45th IEEE Conference on Decision and Control*, 2006, pp. 2693–2697. doi:10.1109/CDC.2006.377210.

[16] Houska, B., and Diehl, M., "Optimal control for power generating kites," *2007 European Control Conference (ECC)*, 2007, pp. 3560–3567. doi:10.23919/ECC.2007.7068861.

[17] Canale, M., Fagiano, L., Ippolito, M., and Milanese, M., "Control of tethered airfoils for a new class of wind energy generator," *2006 45th IEEE Conference on Decision and Control*, 2006, pp. 4020–4026. doi:10.1109/CDC.2006.376775.

[18] Ilzhöfer, A., Houska, B., and Diehl, M., "Nonlinear MPC of kites under varying wind conditions for a new class of large-scale wind power generators," *International Journal of Robust and Nonlinear Control*, Vol. 17, No. 17, 2007, pp. 1590–1599. doi:10.1002/rnc.1210.

[19] Zanon, M., Gros, S., Meyers, J., and Diehl, M., "Airborne Wind Energy: Airfoil-Airmass Interaction," *IFAC Proceedings Volumes*, Vol. 47, No. 3, 2014, pp. 5814 – 5819. doi:10.3182/20140824-6-ZA-1003.00258, 19th IFAC World Congress.

[20] Leuthold, R., Gros, S., and Diehl, M., "Induction in Optimal Control of Multiple-Kite Airborne Wind Energy Systems," *IFAC-PapersOnLine*, Vol. 50, No. 1, 2017, pp. 153 – 158. doi:10.1016/j.ifacol.2017.08.026, 20th IFAC World Congress.

[21] Williams, P., "Optimal Wind Power Extraction with a Tethered Kite," *AIAA Guidance, Navigation, and Control Conference and Exhibit*, American Institute of Aeronautics and Astronautics, 2006. doi:10.2514/6.2006-6193.

[22] Erhard, M., and Strauch, H., "Control of Towing Kites for Seagoing Vessels," *IEEE Transactions on Control Systems Technology*, Vol. 21, No. 5, 2013, pp. 1629–1640. doi:10.1109/TCST.2012.2221093.

[23] Jehle, C., and Schmehl, R., "Applied Tracking Control for Kite Power Systems," *Journal of Guidance, Control, and Dynamics*, Vol. 37, No. 4, 2014, pp. 1211–1222. doi:10.2514/1.62380.

[24] Fagiano, L., Zgraggen, A., Morari, M., and Khammash, M., "Automatic Crosswind Flight of Tethered Wings for Airborne Wind Energy: Modeling, Control Design, and Experimental Results," *IEEE Transactions on Control Systems Technology*, Vol. 22, No. 4, 2014, pp. 1433–1447. doi:10.1109/TCST.2013.2279592.

[25] Fechner, U., "A Methodology for the Design of Kite-Power Control Systems," Dissertation, Delft University of Technology, 2016. doi:10.4233/uuid:85efaf4c-9dce-4111-bc91-7171b9da4b77.

[26] Zgraggen, A. U., Fagiano, L., and Morari, M., "Real-Time Optimization and Adaptation of the Crosswind Flight of Tethered Wings for Airborne Wind Energy," *IEEE Transactions on Control Systems Technology*, Vol. 23, No. 2, 2015, pp. 434–448. doi:10.1109/TCST.2014.2332537.

[27] Costello, S., François, G., and Bonvin, D., "Real-Time Optimizing Control of an Experimental Crosswind Power Kite," *IEEE Transactions on Control Systems Technology*, Vol. 26, No. 2, 2018, pp. 507–522. doi:10.1109/TCST.2017.2672404.

[28] Bauer, F., Kennel, R. M., Hackl, C. M., Campagnolo, F., Patt, M., and Schmehl, R., "Power Curve and Design Optimization of Drag Power Kites," *Book of Abstracts of the Airborne Wind Energy Conference 2017*, edited by M. Diehl, R. Leuthold, and R. Schmehl, Albert Ludwigs University of Freiburg and Delft University of Technology, Freiburg, Germany, 2017, pp. 72–73. doi:10.4233/uuid:4c361ef1-d2d2-4d14-9868-16541f60edc7.

[29] Bauer, F., Kennel, R. M., Hackl, C. M., Campagnolo, F., Patt, M., and Schmehl, R., “Drag power kite with very high lift coefficient,” *Renewable Energy (Elsevier)*, Vol. 118, No. Supplement C, 2018, pp. 290 – 305. doi:10.1016/j.renene.2017.10.073.

[30] van der Vlugt, R., Bley, A., Noom, M., and Schmehl, R., “Quasi-steady model of a pumping kite power system,” *Renewable Energy*, Vol. 131, 2019, pp. 83 – 99. doi:10.1016/j.renene.2018.07.023.

[31] Milutinovic, M., Kranjcevic, N., and Deur, J., “Multi-mass dynamic model of a variable-length tether used in a high altitude wind energy system,” *Energy Conversion and Management*, Vol. 87, 2014, pp. 1141 – 1150. doi:10.1016/j.enconman.2014.04.013.

[32] Burton, T., Jenkins, N., Sharpe, D., and Bossanyi, E., *Wind Energy Handbook*, Wiley, 2011.

[33] Archer, C. L., and Jacobson, M. Z., “Evaluation of global wind power,” *Journal of Geophysical Research: Atmospheres*, Vol. 110, No. D12, 2005. doi:10.1029/2004JD005462.

[34] Argatov, I., Rautakorpi, P., and Silvennoinen, R., “Estimation of the mechanical energy output of the kite wind generator,” *Renewable Energy*, Vol. 34, No. 6, 2009, pp. 1525 – 1532. doi:10.1016/j.renene.2008.11.001.

[35] Argatov, I., Rautakorpi, P., and Silvennoinen, R., “Apparent wind load effects on the tether of a kite power generator,” *Journal of Wind Engineering and Industrial Aerodynamics*, Vol. 99, No. 10, 2011, pp. 1079 – 1088. doi:10.1016/j.jweia.2011.07.010.

[36] Schmehl, R., and van der Vlugt, R., “Traction Power Generation with Tethered Wings – A Quasi-Steady Model for the Prediction of the Power Output,” *Book of Abstracts of the International Airborne Wind Energy Conference 2015*, edited by R. Schmehl, Delft University of Technology, Delft, The Netherlands, 2015, p. 39. doi:10.4233/uuid:7df59b79-2c6b-4e30-bd58-8454f493bb09.

[37] Fagiano, L., “Control of Tethered Airfoils for High-Altitude Wind Energy Generation,” Dissertation, Politecnico di Torino, 2009. URL http://lorenzofagiano.altervista.org/docs/PhD$_t$hesis$_F$agiano$_F$inal.pdf.

[38] Katz, J., and Plotkin, A., *Low-Speed Aerodynamics*, Cambridge Aerospace Series, Cambridge University Press, 2001.

[39] Vander Lind, D., and Jensen, K., “Methods and systems for managing power generation and temperature control of an aerial vehicle operating in crosswind-flight mode,” , Aug. 23 2016.

[40] Venkataraman, B., Godsey, B., Premerlani, W., Shulman, E., Thakur, M., and Midence, R., “Fundamentals of a motor thermal model and its applications in motor protection,” *Conference Record of 2005 Annual Pulp and Paper Industry Technical Conference, 2005.*, 2005, pp. 11–28. doi:10.1109/PAPCON.2005.1502046.

[41] Makani Power, Inc., “Response to the Federal Aviation Authority. Docket No.: FAA-2011-1279; Notice No. 11-07. Notification for Airborne Wind Energy Systems (AWES).” , 2012. URL https://www.regulations.gov/document?D=FAA-2011-1279-0014.

[42] Vander Lind, D., “Kite configuration and flight strategy for flight in high wind speeds,” , 2018. US Patent 9,896,201.